






## Effect of stratification on the mixing and reaction yield in a T-shaped micro-mixer

A. Mariotti , C. Galletti \*, R. Mauri, M. V. Salvetti , and E. Brunazzi   
*Dipartimento di Ingegneria Civile e Industriale, University of Pisa, 56122 Pisa, Italy*

 (Received 14 December 2020; accepted 5 February 2021; published 24 February 2021)

The effect of a small density difference, i.e., lower than 12%, between the two miscible liquid streams fed to a T-shaped junction is investigated experimentally and through numerical simulations. Micron-resolution particle image velocimetry (micro-PIV) experiments provided detailed support to the numerical analysis of how stratification influences flow features in different flow regimes. From dimensional analysis, we find that gravitational and inertial fluxes balance each other at a distance  $L = d/\sqrt{\text{Ri}}$  from the confluence along the mixing channel, where  $d$  is the hydraulic diameter and  $\text{Ri}$  is the Richardson number. In general, at distances  $|y| \ll L$ , the influence of gravity can be neglected, while at  $|y| \gg L$  the two fluids are fully segregated; in particular, at the confluence, the flow field is the same as the one that we obtain assuming that the two inlet fluids are identical. Thus, in the segregated regime, the contact region separating the two fluids of the inlet streams remains vertical at distances  $|y| \ll L$  along the mixing channel while it becomes progressively horizontal at  $|y| \approx L$ . In the vortex regime as well, near the confluence the flow field presents a mirror symmetry, with a very small resulting degree of mixing; however, as we move down the mixing channel, when  $|y| > L$ , gravity becomes relevant, leading to a symmetry breaking that promotes convection and enhances mixing. When we further increase the Reynolds number, in the engulfment regime, the degree of mixing becomes much larger due to the mixing induced by the flow instability at the confluence and thus the successive stratification appears to have a small effect on the flow topology, with a degree of mixing that continues to grow very slowly in the mixing channel, similar to what happens in the case of identical inlet fluids. As expected, the onsets of the vortex and engulfment regimes occur at values of the Reynolds number  $\text{Re}$  that hardly depend on the density difference between the two inlet fluids, provided that  $\text{Re}$  is defined in terms of the fluid properties of a homogeneous fluid mixture. Finally, the reaction yield along the mixing channel is computed both from numerical and experimental data. In agreement with theoretical predictions, we found that the reaction yield depends on the Damköhler number and the kinetic constant, while it is independent of the density ratio, at least within the range of the investigated conditions.

DOI: [10.1103/PhysRevFluids.6.024202](https://doi.org/10.1103/PhysRevFluids.6.024202)

### I. INTRODUCTION

Micro-reactor technology can contribute substantially to the intensification of pharmaceutical and fine-chemistry processes as converting traditional batch operations to continuous flow reactors may lead to a significant increase in the yield and the selectivity of chemical reactions [1]. This can be attributed to the unprecedented control of the operating conditions that micro-reactors provide,

---

\*chiara.galletti@unipi.it

allowing them to fulfill the fundamental principles of process intensification, i.e., the achievement of uniform processing conditions and the optimization of driving forces [2,3].

Despite the recognized benefits and strong expectations of what micro-reactors can offer, their practical application has been limited so far. One critical point is the lack of sufficient throughput to meet the industrial needs, as the desired production rates are difficult to be achieved with just increasing the number of reactors (numbering-up technique) if their dimension is in the range of 50–300  $\mu\text{m}$ . An increase of their size up to the millimeter scale can overcome this problem; hence, in the past decade, milli-reactors have received growing attention [4–6]. Indeed, they can combine benefits of micro-devices, i.e., continuous operation with high control of operating conditions, with the throughput of conventional batch reactors [7].

To perform effectively liquid reactions in micro- and milli-devices, the mixing between reactants should be optimized. The micro-devices are characterized in terms of degree of mixing. This is usually estimated from experiments or numerical simulations which are performed by feeding a single fluid, which often is water, to the mixer, and adding a dye to discern between the fluid streams.

One of the most investigated geometry is the T-shaped micro-mixer, in which the inlet channels join perpendicularly the mixing channel. Despite its basic geometry and the laminar flow, different complex flow regimes occur with increasing the Reynolds number [8], which is usually defined with the hydraulic diameter of the mixing channel,  $d$ , i.e.,  $\text{Re} = \frac{Ud}{\nu}$ . Here  $U$  is the bulk velocity, while  $\nu$  is the kinematic viscosity. For example, lots of works focus on flow regimes occurring when the device is operated with a single fluid fed with equal flow rates to the two inlet channels, the latter have square cross sections, i.e., their width  $W_i$  is equal to their height  $H$ , and the mixing channel has an aspect ratio  $W : H = 2 : 1$ , where  $W$  is the mixing channel width, i.e., the bulk velocity is constant. For such configuration and for low  $\text{Re}$ , the flow is steady and segregated, with the two fluid streams entering the mixer and flowing aside along the mixing channel (*segregated regime*). Then, with increasing the flow rate, three-dimensional (3D) U-shaped vortical structures originate at the confluence between the inlet streams, leading to a double pair of counter-rotating legs in the mixing channel (steady symmetric or vortex regime). When further increasing  $\text{Re}$ , we observe a tilting of the top part of the U-shaped vortical structures, resulting in one of their two legs being more fed by the incoming fluid than the other (steady asymmetric or engulfment regime). Consequently, in the mixing channel only the two strongest legs, which are corotating, survive, while the two weaker legs soon disappear. The loss of reflectional symmetry leads to a remarkable increase of the degree of mixing and hence the engulfment regime has been largely investigated for practical reasons [9–11]. When we further augment  $\text{Re}$ , the flow becomes unsteady and time periodic, with a large degree of asymmetry (periodic asymmetric regime) boosting mixing, which can be up to 30–50% larger than that provided by the engulfment regime [12]. However, the additional increase of  $\text{Re}$  leads to a flow, which, although still time periodic, shows unexpectedly a large degree of symmetry, resulting in a detrimental effect on mixing (periodic symmetric regime). Finally, when we further increase  $\text{Re}$  the flow becomes chaotic.

The literature is very extensive, with numerous experimental and numerical investigations analyzing the effect of operating conditions [13], working fluids [14,15], geometry (e.g., channel aspect ratio [16–20], angle of the inlet channels [21–24], staggered, offset inlets [25], or curved micro-channels [26]) on the flow regimes and how they do affect ultimately the degree of mixing.

However, one aspect that is generally neglected is the effect of gravity, which may lead to a stratification of the incoming fluid streams when they have different densities. Logically, this issue has not been taken into account because, as mentioned above, in most previous investigations the same fluid is used in both inlets, and a dye is added which does not alter the fluid properties. However, the practical application of micro- and milli-reactors is likely to involve a density difference between the reactants, as, for instance, in case of aqueous-organic solvent mixtures (e.g., water-ethanol [27,28]), which are often employed in chemical reactions or in nano- and micro-particle synthesis. Moreover, density differences may stem from feeding streams that are the same fluid but with different temperatures [29,30].

Even though in micro-reactors gravity has often been neglected, in the case of milli-reactors gravity may play a role even for limited density ratios, because of the slower velocity and higher residence time for the same Re number. In addition, if we imagine serpentine micro-reactors [31,32], where the serpentine shape allows enough residence time for reaction, we may expect stratification to have time to develop.

So the issues here are the following: Does gravity affect flow regimes and hence mixing in the case of miscible liquids showing a density difference? Can the findings on flow regimes discussed in the literature be applied straightforwardly to cases presenting a density difference or do we need to pay attention to this aspect? Does a density difference affect the reaction yield?

Recently, Lobasov and Minakov [33] performed numerical simulations of a T-shaped micro-mixer fed with two miscible liquids having a large density ratio, i.e., equal to 2, and took into account gravity, which was directed downward the mixer height. They simulated different micro-mixers, all of them with square inlets and an aspect ratio of the mixing channel  $W : H = 2 : 1$ , but varying mixer heights in the range 100–400  $\mu\text{m}$ . They considered two different Reynolds numbers, i.e.,  $\text{Re} = 120$  and  $\text{Re} = 180$ , for which the flow was in the vortex and engulfment regime, respectively. Gravity was found to have a negligible effect on the concentration field at the outlet of the mixer, i.e., after  $10d$ , for the smaller micro-mixer sizes, with just a little change of the shape of the contact region between the two fluid streams that could be seen in the case of  $H = 200 \mu\text{m}$ . Instead, for the larger micro-mixers, with  $H = 300 \mu\text{m}$  and  $H = 400 \mu\text{m}$ , a noticeable effect was observed, with the denser fluid moving toward the bottom of the mixing channel and the lighter moving upward. The resulting degree of mixing was found to be affected by gravity in both the vortex and engulfment regimes.

In a recent paper [34], we have experimentally and numerically investigated mixing and reaction in a T-shaped mixer having  $W_i = H = 1000 \mu\text{m}$  and  $W = 2H$  for Reynolds numbers in the range  $\text{Re} = 10\text{--}280$ . Specifically, as the progress of the chosen reaction was accompanied by decolorization, experimental flow visualizations were used to acquire the reaction yield along the mixing channel. Numerical simulations provided further details, allowing us not only to confirm the values of reaction yield but also to analyze the flow features. In particular, numerical predictions indicated that despite the fact that the reactants had a small density difference, i.e., the density ratio was 1.117, stratification affected the characteristics of the flow regimes at low Re. In the segregated regime, the separation region between the fluid streams moved from vertical to inclined and horizontal while proceeding along the mixing channel, with the denser fluid moving toward the bottom of the channel. This behavior is in contrast with that of a single fluid exhibiting a perfectly vertical contact region. At higher Re in the vortex regime, the vortical structures on the two sides of the mixing channel had different intensities because of the different properties of the incoming streams; thus, the double mirror symmetry, which is typical of the single-fluid case, was lost. This behavior has a beneficial effect on mixing, which is improved. Conversely, in the engulfment regime, the flow behaved similarly to the single-fluid case, with only small effects of flow stratification. Moreover, in the aforementioned work, we showed that the reaction yield,  $\eta = 1 - 2 \frac{C_{X,\text{out}}}{C_{X,\text{in}}}$ , with  $C_{X,\text{out}}$  and  $C_{X,\text{in}}$  being the concentrations of the considered reactant averaged at the reference outlet and inlet sections, respectively, in the segregated regime depends solely on the flow to chemical timescale ratio, i.e., Damköhler number  $\text{Da} = dk_{r,0}/U$  where  $k_{r,0}$  is the kinetic constant obtained for the nominal concentrations of the reactants, as  $\eta \propto \text{Da}^{0.3}$ . Conversely, in the vortex and engulfment regimes, an explicit dependency on the kinetic constant was observed because of the enhanced mixing as  $\eta \propto \frac{\tilde{k}_{r,0}^{0.1}}{\text{Da}^{0.4}}$ , with  $\tilde{k}_{r,0} = k_{r,0} \frac{d^2}{\nu}$  being a nondimensional kinetic constant taking into account also fluid properties and hydraulic diameter  $d$ .

The present work is aimed at further elucidating the above findings and extending them to different conditions in terms of density ratios and kinetic constants. First, we want to validate numerical predictions with a detailed experimental analysis of the flow field based on the Micron-resolution particle image velocimetry (micro-PIV) technique to provide experimental evidence of stratification in a micro-T junction. Second, we want to understand what happens for even smaller

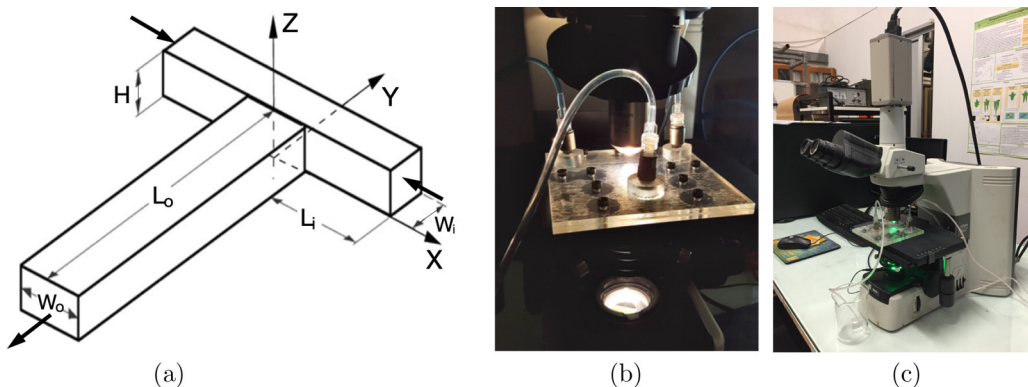


FIG. 1. (a) Sketch of the T-reactor geometry and reference system; (b) picture of the T reactor; and (c) PIV setup.

density differences than those in Ref. [34]. The size of the device, i.e.,  $W_i = H = 1000 \mu\text{m}$ , will enable us to gain insight into the stratification for quite large microreactors, i.e., approaching the millimeter scale, to be used in practical applications. Ultimately, we intend to critically analyze the applicability of the scaling of the reaction yield with Damköhler number and kinetic constant proposed in Mariotti *et al.* [34] by the extending test cases. To this purpose, we have considered a significant range of variation of the kinetic constant values. On the other hand, we also managed to get the same kinetic constant with different density ratios to single out the effect of stratification.

T-reactor geometry, chemicals, and experimental setup are presented in Sec. II, whereas numerical methodology and simulation setup are described in Sec. III. The different flow regimes occurring in the T reactor are shown in Sec. IV, and stratification effects on mixing performance and reaction yield are discussed in Sec. VI.

## II. EXPERIMENTAL SETUP

### A. T reactor and chemicals

The T-shaped micro-reactor consists of three layers made of polymethylmethacrylate (PMMA). The three layers are sealed by using two double-sided adhesive films and screws. The central layer, having a thickness equal to 1 mm, has a T-shaped cut through. The top and bottom layers, 3 mm thick, allow optical access and are equipped with fluidic connections. The T-reactor geometry is shown in Fig. 1(a), together with the adopted reference system, whereas a picture of the device can be seen in Fig. 1(b). The T-reactor dimensions are the same as those used by Mariotti *et al.* [34] and are briefly recalled herein. The inlet channels are characterized by a square cross section, with  $W_i = H = 1 \text{ mm}$ , while the mixing channel has a rectangular cross section with aspect ratio 2:1, i.e.,  $W_o = 2H = 2 \text{ mm}$ . The hydraulic diameter of the mixing channel is  $d = 4H/3$ . In the rest of the paper, coordinates will be made nondimensional by using the hydraulic diameter, i.e.,  $X = x/d$ ,  $Y = y/d$ , and  $Z = z/d$ . The length of the inlet channels is equal to  $L_i = 40 \text{ mm} \cong 30d$ , in order to have a fully developed flow at the T junction, whereas the mixing channel length is equal to  $L_o = 60 \text{ mm} \cong 45d$  to assure the evolution of vortical structures in the mixing channel [34].

The test reaction is the reduction of methylene blue ( $\text{MB}^+$ ) to the colorless leucomethylene blue ( $\text{LMB}^+$ ) by means of ascorbic acid (AsA) and catalyzed by hydrogen chloride (HCl), via the two following parallel reactions [34]:

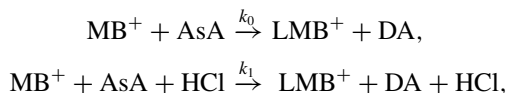


TABLE I. Test matrix and pseudo-first-order kinetic constants  $k_{r,0}$  obtained for the different nominal concentrations of AsA and HCl.

Test	AsA [mol/L]	HCl [mol/L]	$k_{r,0}$ [1/s]
1	0.85	0.10	1.30
2	0.85	0.39	2.60
3	0.85	2.19	10.71
4	1.7	0.10	2.60
5	1.7	1.00	10.71
6	1.7	2.19	21.43

where DA is the dehydroascorbic acid. Therefore, indicating by square brackets the molar concentrations (in mol/L), we have

$$\frac{d[\text{MB}^+]}{dt} = \frac{d[\text{AsA}]}{dt} = -\frac{d[\text{DA}]}{dt} = -\frac{d[\text{LMB}^+]}{dt} = -k_r[\text{MB}^+], \quad \frac{d[\text{HCl}]}{dt} = 0, \quad (1)$$

where  $k_r = (k_0 + k_1[\text{HCl}])([\text{AsA}])$ .

The reaction kinetics was studied experimentally at room temperature by Mowry and Ogren [35], who found the following reaction rates:  $k_0 = 1 \text{ L mol}^{-1} \text{ s}^{-1}$  and  $k_1 = 5.3 \text{ L}^2 \text{ mol}^{-2} \text{ s}^{-1}$ . We see that in case of an excess of ascorbic acid, i.e., when  $[\text{AsA}] \gg [\text{MB}^+]$  as in the present case, the reaction is a pseudo-first-order reaction that depends on the concentration of  $\text{MB}^+$  only, while the kinetic constant,  $k_r$ , can be varied using different concentrations of HCl (see Ref. [34] for more details).

The two reactants enter the reactor from the two inlet channels. The aqueous solution of  $\text{MB}^+$  and HCl enters from one inlet, while the aqueous solution of AsA is fed into the other inlet. 17 mg/L of  $\text{MB}^+$  powder (by Sigma Aldrich) are dissolved in aqueous solutions of HCl (by Sigma Aldrich) to prepare the solutions of  $\text{MB}^+$  and HCl. The corresponding concentration of  $\text{MB}^+$  is thus fixed and equal to  $[\text{MB}^+] = 5.31 \times 10^{-5} \text{ mol/L}$ . On the other hand, different concentrations of HCl are considered in the range  $[\text{HCl}] = 0.1\text{--}2.19 \text{ mol/L}$ . As for the aqueous solutions of ascorbic acid, 150 and 300 mg/L of L-ascorbic acid (Ultrafine vitamin C powder by Cutatonic) are dissolved in deionized water, to obtain ascorbic acid concentrations equal to  $[\text{AsA}] = 0.85$  and  $[\text{AsA}] = 1.7 \text{ mol/L}$ , respectively. Table I summarizes the test matrix and the pseudo-first-order kinetic constants,  $k_{r,0}$ , obtained for the different nominal concentrations of AsA and HCl, whereas the physical properties of the working fluids are reported in Table II as a function of ascorbic acid concentration.

A KD Scientific syringe pump Gemini 88, equipped with two Becton Dickson plastic syringes of 60 mL, was used to introduce the two streams at the same flow rate. The pump is stopped after each test and then started again, imposing the new flow rate. This procedure is aimed at avoiding any hysteresis phenomena in the mixing and reaction process.

## B. Particle image velocimetry, flow topology, and reaction yield measurements

Particle image velocimetry (PIV) was used to gain insight in the flow structure. A planar two-component setup is adopted to investigate different planes normal to the  $z$  direction. A field of view

TABLE II. Physical properties of the working fluids.

	$\rho$ [g/cm <sup>3</sup> ]	$\mu$ [mPa s]	$\nu$ [mm <sup>2</sup> /s]
Water	1	1	1
[AsA] = 0.85 mol/L	1.058	1.003	1.19
[AsA] = 1.7 mol/L	1.117	1.7	1.52

covering the whole T-junction region is chosen, having dimensions  $2.325d \times 1.77d$ , where  $d$  is the hydraulic diameter of the mixing channel. The field of view is imaged by an upright microscope model Nikon Eclipse 80i equipped with a magnifying lens of  $4\times$  having a Numerical Aperture equal to  $N.A. = 0.13$ . A Dantec Microstrobe light source is used as a volume illumination and the microscope objective's depth of field determines the thickness of the measurement volume. The Dantec Microstrobe is a pulsed light source, and the time interval between two subsequent pulses can be set between  $10\ \mu\text{s}$  and  $10\ \text{ms}$ . The emitted light has a wavelength of  $530\ \text{nm}$ . For the Reynolds numbers considered in the present work, i.e.,  $Re = 10\text{--}150$ , the time between two subsequent pulses is set in the range  $\Delta t = 100\text{--}550\ \mu\text{s}$ , depending on the Reynolds number. These intervals have been chosen to have an appropriate displacement of tracers for obtaining reliable PIV data. According to Ref. [36], the thickness of the measurement volume can be estimated equal to  $0.125d$ ; thus, up to nine measurements planes can be distinguished in the T-reactor depth.

The two entering streams are seeded with Molecular Probes Fluospheres, carboxylate-modified microspheres, Nile red fluorescent, having diameters of  $1\ \mu\text{m}$ . The images are collected by using the Digital CCD Camera C8484-05C-Hamamatsu, having a rectangular monochrome sensor with a resolution of  $1344 \times 1024$  pixels, with a high sensitivity in the visible and infrared light spectrum. In front of the camera, a  $0.7\times$  lens is mounted to collect a region of  $2.325d \times 1.77d$  in a single image (the equivalent dimension of a pixel is  $2.3\ \mu\text{m}$ ). A picture of the experimental setup is shown in Fig. 1(c). For each configuration studied, a total of 200 image pairs are acquired at a rate of  $6.1\ \text{Hz}$  (arbitrarily chosen since the flow is steady), which was found satisfactory for convergence of the second-order statistics. Image pairs are processed with Dantec adaptive PIV tools using a final interrogation window of  $16 \times 16$  pixels and overlap of  $50\%$ , leading to a spacing equal to  $0.028d$  of the velocity vectors in the collection region. To improve the signal-to-noise ratio, during the preprocessing of the images (before the correlation), we first subtract the background from the PIV recorded images to reduce the background noise. Moreover, thanks to adaptive PIV techniques, the signal-to-noise ratio is improved by balancing the use of results from small interrogation areas ( $8 \times 8$  pixels), having high spatial resolution and lower signal-to-noise ratio, and increasing the size of the correlation windows (up to  $64 \times 64$  pixels), having higher signal-to-noise ratio and reduced spatial resolution. At the end of this adaptive procedure, image pairs are presented in the paper using a final interrogation window of  $16 \times 16$  pixels. In addition to this, spurious vectors due to insufficient seeding particle density are eliminated. All the experiments were performed in a dark room in order to maintain a constant level of luminosity and to minimize any reflection and shadow.

The flow topology and the progress of the reaction at the confluence region and along the mixing channel were also evaluated. The setup is the same as that in Ref. [34] and it is briefly recalled herein. For these measurements, a high-speed camera Optomotive Velociraptor HS was used to collect the images. The high-speed camera has a  $2048 \times 2048$  pixels monochrome sensor, and the light source is a D-LH 12V-100W halogen lamp. The maximum frame rate of the camera is  $387\ \text{frames/s}$  when the sensor resolution is reduced to  $920 \times 2048$  pixels. In front of the camera a  $0.5\times$  lens is mounted to collect a region of  $1.8d \times 4d$  in a single image (the equivalent dimension of a pixel is  $2.6\ \mu\text{m}$ ).

The images acquired by the high-speed camera allowed us to analyze the color-fading reaction. Among the species involved in the reaction,  $\text{MB}^+$  is the only light-absorbing species. Therefore, the resulting intensity of the light across the specimen that is captured by the camera depends only on the  $\text{MB}^+$  concentration. The relationship between the  $\text{MB}^+$  concentration and light absorbance is preliminarily assessed through calibration runs, performed by filling the reactor with various sample solutions of known levels of  $\text{MB}^+$  concentration in the range  $0\text{--}6.25 \times 10^{-5}\ \text{mol/L}$ . Using the same procedure as in Ref. [34], the light intensity of each set of acquired images (100 images per set) is analyzed pixel by pixel for all these sample solutions to estimate the relationship of light absorbance with concentration for every individual pixel in the image. The results were found to be in good agreement with the Lambert-Beer's linear relationship between the  $\text{MB}^+$  concentration and light absorbance. Thus, normalized depth-averaged  $\text{MB}^+$  concentration distributions were obtained from

the light-intensity images by applying the following equation in each  $(ij)$ th pixel of the images:

$$\frac{\ln(I_{\text{blank},ij}) - \ln(I_{k,ij})}{\ln(I_{\text{blank},ij}) - \ln(I_{\text{max},ij})} = \frac{C_{k,ij}}{C_0}, \quad (2)$$

where  $I_{k,ij}$  is the instantaneous value of the light intensity,  $C_{k,ij}$  is the instantaneous value of the  $\text{MB}^+$  concentration,  $I_{\text{blank},ij}$  is the value of light intensity acquired when the mixer is full of only the blank solution, and  $C_0$  is the concentration when the mixer is full of the  $C_0 = 5.3 \times 10^{-5} \text{ mol/L MB}^+$  solution. The reference values of  $I_{\text{blank},ij}$  and  $I_{\text{max},ij}$  are measured for each set of experiments, before using the two streams together. These references are evaluated as the arithmetic mean values over 80 frames each to reduce the effects of undesirable time fluctuation of pixel intensity. During the reaction experiments,  $I_{k,ij}$  are computed from 600 images with a frame rate of 387 frames/s for each considered Re value. Postprocessing of the images was carried out through an off-line automatized procedure that was developed to directly convert pixel intensity maps into distributions of normalized depth-averaged  $\text{MB}^+$  concentration [11].

The two streams are characterized by slightly different refractive indexes, viz. 1.33 for the  $\text{MB}^+$  solution and 1.36–1.37 for the AsA solution [37]. The optical rays in their course across the specimen are somewhat diverted due to refraction resulting from the differences in the refractive indexes. Thus, darker or brighter streaks compared to the rest of the image were observed at the contact fronts of the two different solutions. The presence of these streaks in the acquired images was minimized by proper focusing of the microscope (with regard to height in relation to the objective) and aperture adjustments of the condenser and the field diaphragms. Streaks minimization was necessary to avoid offsetting the concentration measurement during the visualizations of the reaction yields. On the contrary, streaks were deliberately highlighted to visualize the flow topology.

### III. NUMERICAL MODEL

Navier-Stokes equations for a steady and variable density flow and transport/reaction equations for  $\text{MB}^+$ ,  $\text{LMB}^+$ , AsA, HCl, and DA are used to describe mixing and reaction in the T-shaped device. The governing equations in isotherm conditions are derived in nondimensional form by normalizing lengths with the mixing channel hydraulic diameter  $d$  and velocities with the inlet bulk velocity  $U$ , as follows:

$$\nabla \cdot (\hat{\rho} \mathbf{u}) = 0, \quad (3)$$

$$\hat{\rho} \mathbf{u} \cdot \nabla \mathbf{u} = -\nabla p + \frac{1}{\text{Re}} \nabla \cdot [\hat{\mu} (\nabla \mathbf{u} + \nabla \mathbf{u}^T)] + \text{Ri} (\hat{\rho} - 1) \hat{\mathbf{g}}, \quad (4)$$

$$\mathbf{u} \cdot \nabla \phi_k = \frac{1}{\text{Pe}} \frac{1}{\hat{\rho}} \nabla \cdot (\hat{\rho} \hat{\mathcal{D}}_k \nabla \phi_k) + \frac{d \dot{\omega}_k}{\rho U}, \quad (5)$$

where  $\mathbf{u}$  is the velocity vector,  $p$  represents the modified nondimensional pressure, i.e.,  $p = (P - \rho_0 g Z) / \rho_0 U^2$ , where  $P$  is the dimensional pressure,  $Z$  is the vertical coordinate (see Fig. 1), and  $g$  is the gravity acceleration, while  $\hat{\mathbf{g}}$  is the nondimensional gravity, i.e.,  $\hat{\mathbf{g}} = \frac{\mathbf{g}}{g}$ . In addition,  $\hat{\rho} = \rho / \rho_0$  and  $\hat{\mu} = \mu / \mu_0$  are nondimensional density and viscosity, respectively, referred to a convenient reference state; in our case,  $\mu_0$  and  $\rho_0$  correspond to density and viscosity of pure water at 20°C. Both density and viscosity are functions of temperature (here constant) and mixture composition only. Finally, in Eq. (5),  $\phi_k$  represents the mass fraction of the  $k$ th chemical species (in  $\text{gL}^{-1} \text{s}^{-1}$ ),  $\dot{\omega}_k$  is its rate of production or consumption due to chemical reactions, and  $\hat{\mathcal{D}}_k = \mathcal{D} / \mathcal{D}_0$  is the nondimensional diffusivity, referred to the diffusivity of pure water,  $\mathcal{D}_0$ . The assumption of steady flow is justified by the fact that we are investigating Reynolds number values for which the flow is steady, as confirmed by the experiments.

In the above equations, the characteristic nondimensional numbers are the Reynolds number  $\text{Re} = \frac{\rho_0 U d}{\mu_0}$ , the Richardson number  $\text{Ri} = \frac{g d \Delta \rho}{\rho_0 U^2}$ , and the Peclet number  $\text{Pe} = \frac{U d}{\mathcal{D}_0}$ , where  $\nu_0 = \mu_0 / \rho_0$

denotes the kinematic viscosity of water, while  $\Delta\rho$  is the density difference between the two inlet fluids. Moreover, a Damköhler number can be defined for each chemical species as the ratio between the production and consumption rates and the convective flux in the mixing channel  $Da_k = d\dot{\omega}_k/U\rho\phi_k$ .

Considering that Eq. (1) indicates a pseudo-first-order reaction in  $[MB^+]$  in the case of an excess of ascorbic acid, with reaction rate  $k_r$ , we obtain

$$\dot{\omega}_{MB^+} = -k_r\omega_{MB^+} = -k_r\rho\phi_{MB^+}, \quad (6)$$

where  $\dot{\omega}_{MB^+}$  is the rate of production or consumption of  $MB^+$  due to chemical reactions and  $\omega_{MB^+} = \rho\phi_{MB^+}$  is the mass concentration of  $MB^+$  (in g/L).

By substituting Eq. (6) into Eq. (5) and defining  $\hat{k}_r = k_r/k_{r,0}$ , where  $k_{r,0}$  is a reference reaction rate (see Table I), the transport and reaction equation for  $MB^+$  can be written as

$$\mathbf{u} \cdot \nabla \phi_{MB^+} = \frac{1}{Pe} \frac{1}{\hat{\rho}} \nabla \cdot (\hat{\rho} \nabla \phi_{MB^+}) - \hat{k}_r Da \phi_{MB^+} \quad (7)$$

with  $Da = d\dot{\omega}_{MB^+}/U\rho\phi_{MB^+} = dk_{r,0}/U$ . Since  $\hat{k}_r$  depends on  $[AsA]$  and  $[MB^+]$ , we need to consider analogous equations for  $\phi_{AsA}$  and  $\phi_{HCl}$ , with corresponding Damköhler numbers that can be derived from Eq. (1), obtaining  $Da_{HCl} = 0$  and  $Da_{AsA} = Da_{MB^+}[MB^+]/[AsA]$ . This shows that reaction is null for HCl, while it is negligible for AsA, since  $[AsA] \ll [MB^+]$ .

Both density and viscosity are taken to be functions of the mass fraction of AsA,  $\phi_{AsA}$ , as [38]

$$\mu = \mu_o(1 + 1.0605\phi_{AsA} + 5.7219\phi_{AsA}^2), \quad (8)$$

$$\rho = \rho_o(1 + 0.39070\phi_{AsA} + 0.1617\phi_{AsA}^2). \quad (9)$$

The same computational domain as in the experiments is considered. In each cell of the computational domain, the mass fractions  $\phi$  of all the reactants and products are considered for the determinations of the above described quantities. Uniform velocity and concentration of the reactants are imposed at the entrance of the inlet channels as their lengths allow the flow to fully develop before the T junction. A pressure outlet condition with ambient pressure is set at the mixer outlet while no-slip velocity is given at the channel walls.

ANSYS FLUENT v. 19, based on the finite volume method, was used to solve the above set of equations with a SIMPLE algorithm for pressure-velocity coupling and second-order upwind interpolations. At convergence, the normalized residuals were all below  $10^{-9}$  and the  $MB^+$  concentration, which was monitored in four locations in the mixing channel, did not change anymore with iterations.

A fully structured grid with 4.7 million cells was used for the initial runs, but then it was refined in regions of high reaction rates. In particular, three mesh-adaption cycles were employed, leading to final grids with number of elements ranging from 10 000 000 to 12 000 000 cells. More details on the mesh adaption and numerical setup are provided in Ref. [34].

#### IV. STRATIFICATION EFFECTS ON FLOW FEATURES

In the work of Mariotti *et al.* [34], we observed for the case with  $[AsA] = 1.7$  mol/L (corresponding to a density ratio of 1.117) in the segregated regime, at  $Re \leq 60$  (based on the water properties), the streams progressively stratify in the mixing channel, with the denser fluid moving toward the bottom of the channel and the lighter fluid moving upwards. Figure 2 visualizes the two streams in the segregated regime at  $Re = 20$  for different density ratios, i.e., 1 (water-water case), 1.058 (ascorbic acid content of  $[AsA] = 0.85$  mol/L) and 1.117 ( $[AsA] = 1.7$  mol/L). Mariotti *et al.* [34] emphasized that the mixture properties depend mainly on the ascorbic acid content, while the HCl concentration has a negligible influence on the flow patterns for the investigated range of compositions. Hence, here we will show flow features only for the lowest acid concentration, i.e.,  $[HCl] = 0.10$  mol/L. The  $MB^+$  concentration predicted by numerical simulations is reported in



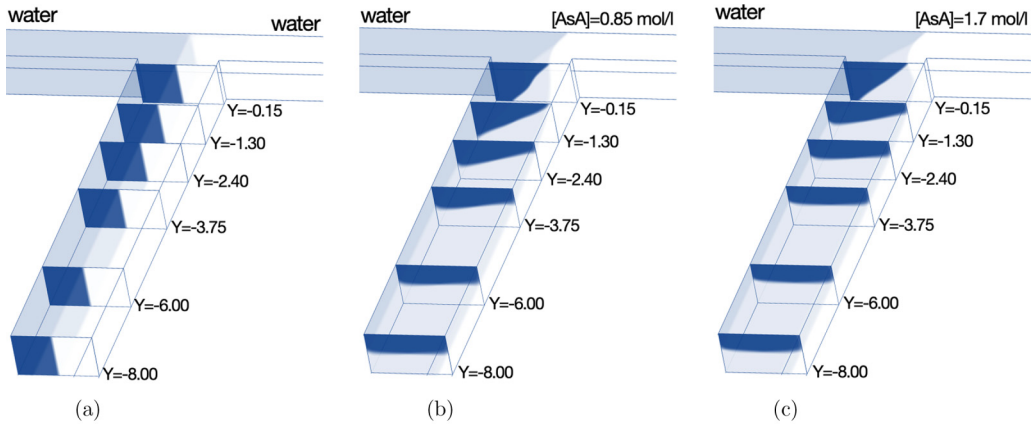


FIG. 2. Numerical nondimensional  $\text{MB}^+$  concentration in different cross sections of the mixing channel at  $\text{Re} = 20$  for  $-8 < Y < -0.15$ . Results for (a) water-water, (b)  $[\text{AsA}] = 0.85 \text{ mol/L}$  and  $[\text{HCl}] = 0.10 \text{ mol/L}$ , and (c)  $[\text{AsA}] = 1.7 \text{ mol/L}$  and  $[\text{HCl}] = 0.10 \text{ mol/L}$ .

different cross sections of the mixing channel for  $-8 < Y < -0.15$ . Such a concentration is made nondimensional by using the  $\text{MB}^+$  concentration in the inlet channel.

For the water-water case, the two streams flow side by side in the mixing channel and the interface is perfectly vertical, i.e., parallel to the side walls of the mixing channel [see Fig. 2(a)]. Despite the small density difference between the streams for  $[\text{AsA}] = 0.85 \text{ mol/L}$ , we clearly see from Fig. 2(b) that stratification takes place. Indeed, the aqueous solution of ascorbic acid (white stream, incoming from the right) moves toward the bottom of the micro-device, being denser than the methylene blue aqueous solution (shown as dark blue on the cross section and light blue in the rest of the device, entering the mixing channel from the left) which tends to occupy the upper part of the channel. We notice how with increasing the density ratio (see Fig. 2(c) for  $[\text{AsA}] = 1.7 \text{ mol/L}$ ), stratification occurs more upstream in the mixing channel. In fact, although in small micro-devices stratification was not observed even with a density ratio of 2 [33], stratification effects are significant also for very small density ratios in devices having dimensions approaching the millimeter, as the ones considered in the present work.

Particle image velocimetry is applied here to measure the velocity field and to provide experimental support to the numerical simulations carried out in the present work and the ones by Mariotti *et al.* [34]. Figure 3 shows the comparison between experimental and numerical results on the horizontal midplane of the microreactor, i.e., for  $Z = 0.375$ . Results for water-water,  $[\text{AsA}] = 0.85 \text{ mol/L}$  and  $[\text{AsA}] = 1.7 \text{ mol/L}$  are compared. The velocity fields are made nondimensional through the bulk velocity  $U$ . The left and middle panels report the distribution of the  $x$  velocity and  $y$  velocity, respectively, while the right panel shows the in-plane velocity magnitude and flow streamlines. The figures show a remarkable agreement between measured and predicted velocity fields for all three cases. For the water-water case [see Fig. 3(a)], the flow field in the horizontal midplane shows a perfect mirror symmetry with respect to the vertical midplane [see the flow streamlines in the right side of Fig. 3(a)]. With increasing density ratios, as we move downward along the mixing channel this symmetry is lost, with the stream coming from the right occupying a slightly larger region in the horizontal midplane [see the streamlines of Figs. 3(b) and 3(c)].

Differences in the flow patterns between the considered working fluids become more evident when we analyze the velocity fields on the horizontal planes at  $Z = 0.525$  and  $Z = 0.675$  shown in Figs. 4 and 5, respectively. Again, nondimensional velocity fields experimentally measured and predicted through numerical simulations for water-water,  $[\text{AsA}] = 0.85 \text{ mol/L}$  and  $[\text{AsA}] = 1.7 \text{ mol/L}$ , are considered. As the density ratio changes, the interface between the two fluids, which is

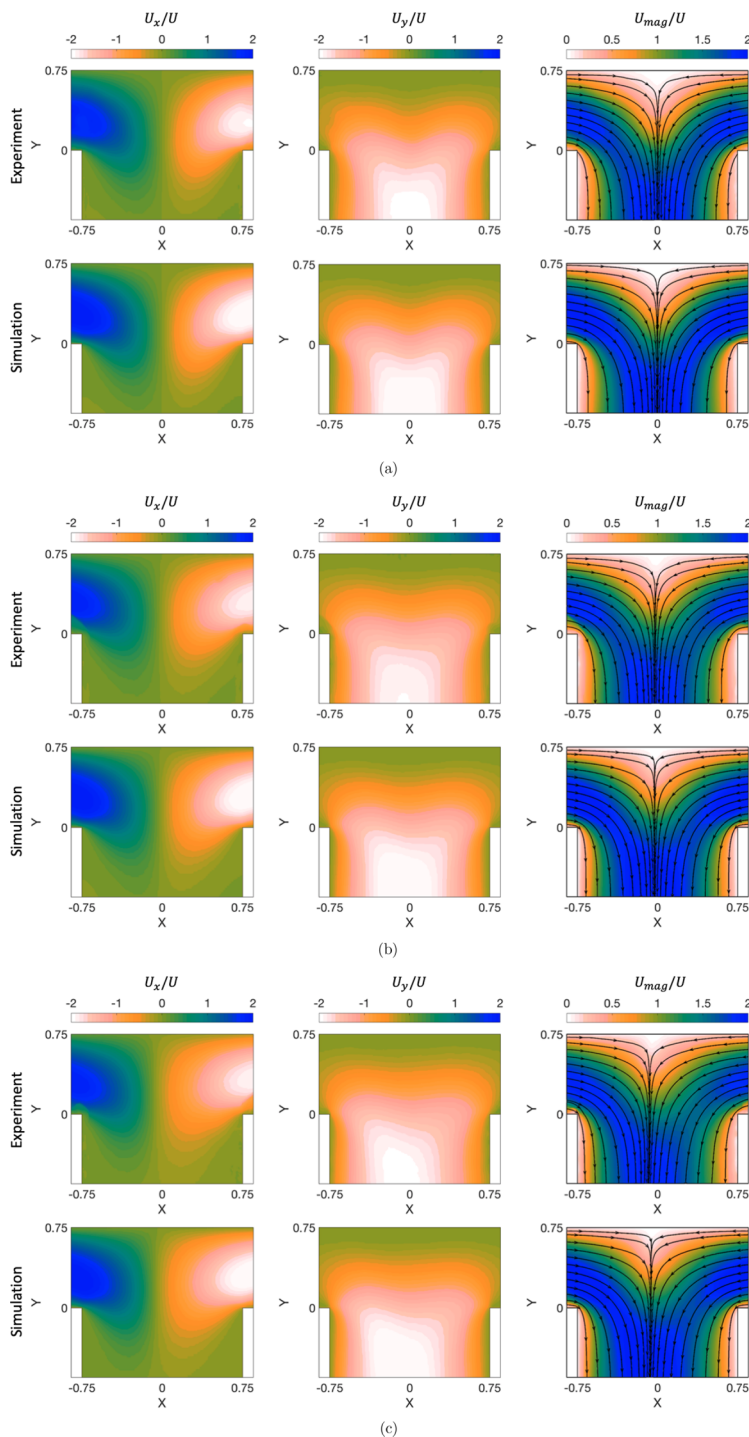


FIG. 3. Nondimensional velocity fields experimentally measured (top) and numerically predicted (bottom) on the plane  $Z = 0.375$ .  $x$ -velocity field (left panel),  $y$ -velocity field (central panel), and velocity magnitude and streamlines (right panel). Results for  $Re = 20$  and (a) water-water, (b)  $[AsA] = 0.85$  mol/L and  $[HCl] = 0.10$  mol/L, and (c)  $[AsA] = 1.7$  mol/L and  $[HCl] = 0.10$  mol/L.

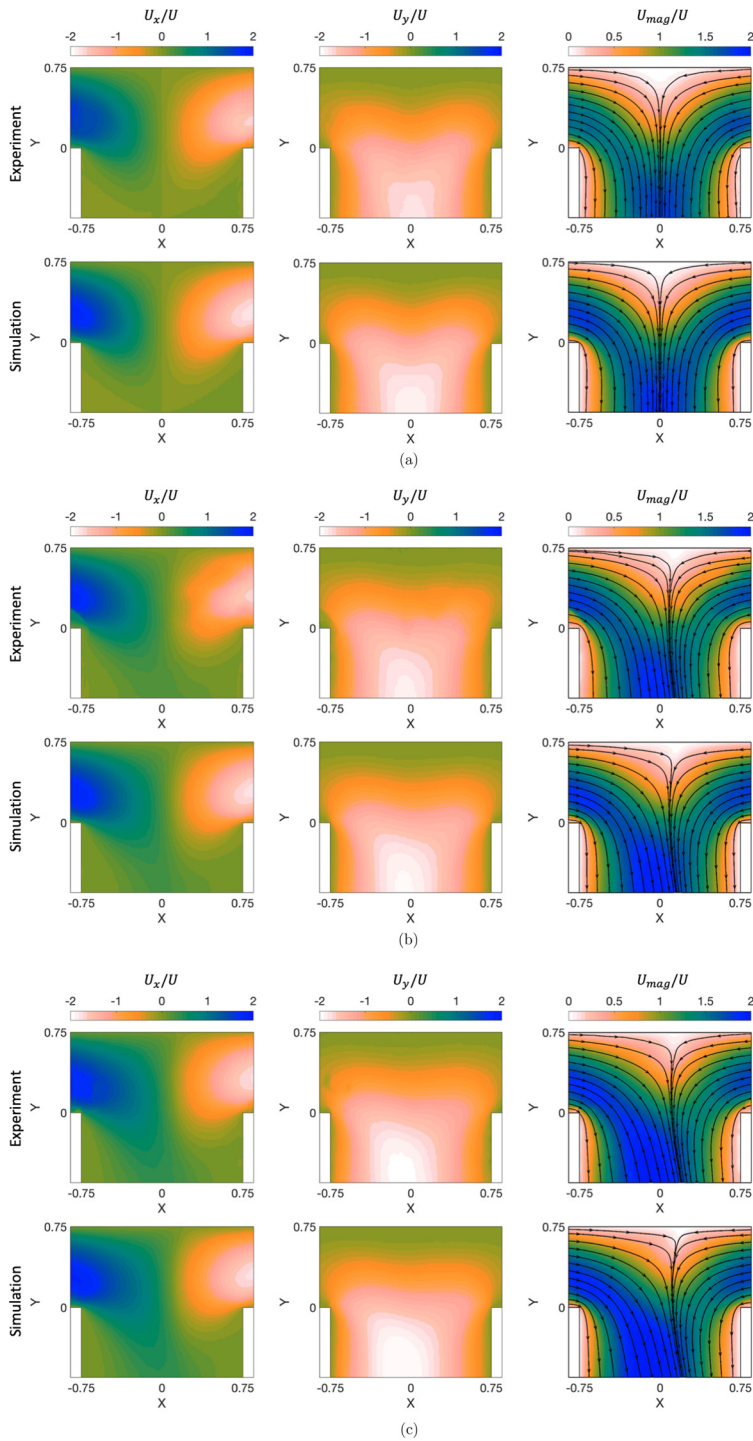


FIG. 4. Nondimensional velocity fields experimentally measured (top) and numerically predicted (bottom) on the plane  $Z = 0.525$ .  $x$ -velocity field (left panel),  $y$ -velocity field (central panel), and velocity magnitude and streamlines (right panel). Results for  $Re = 20$  and (a) water-water, (b)  $[AsA] = 0.85$  mol/L and  $[HCl] = 0.10$  mol/L, and (c)  $[AsA] = 1.7$  mol/L and  $[HCl] = 0.10$  mol/L.

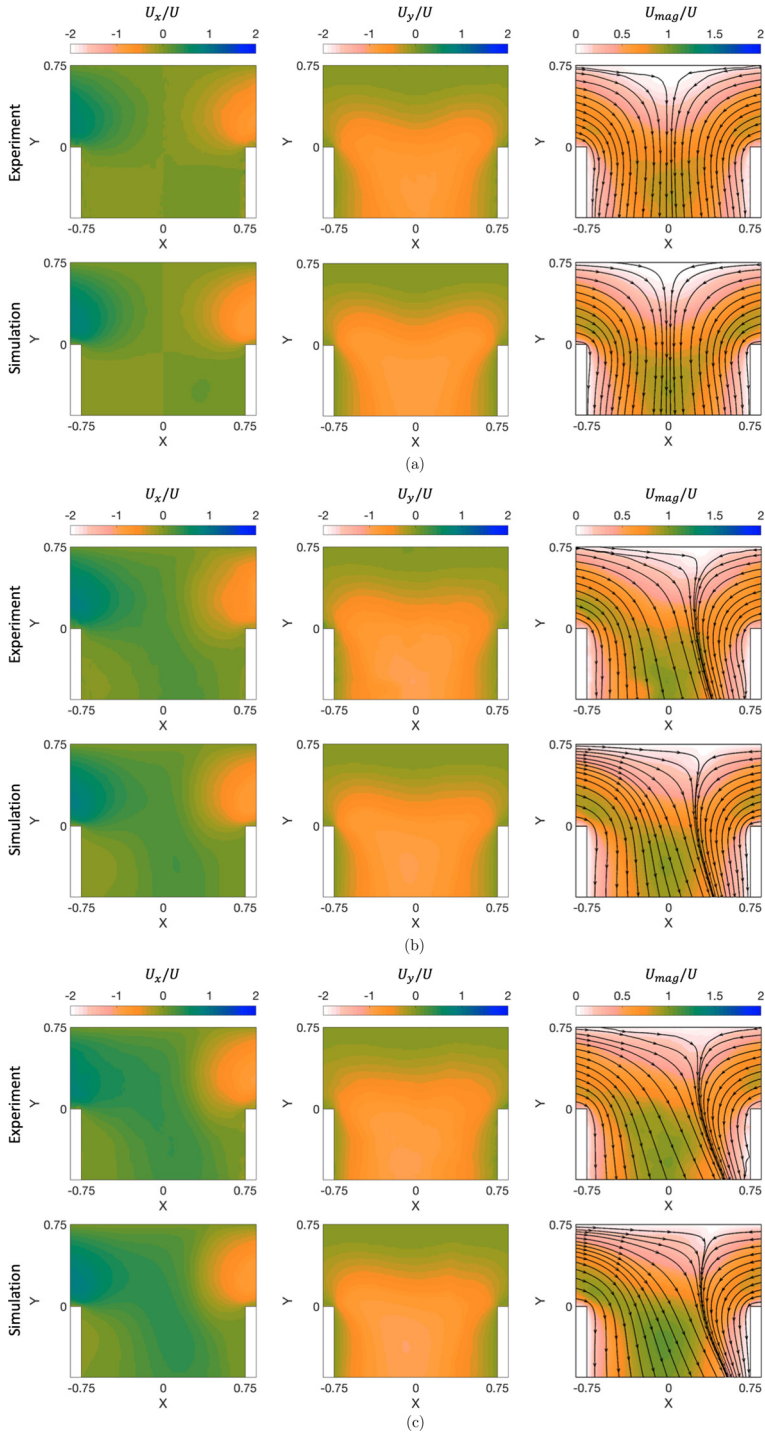


FIG. 5. Nondimensional velocity fields experimentally measured (top) and numerically predicted (bottom) on the plane  $Z = 0.675$ .  $x$ -velocity field (left panel),  $y$ -velocity field (central panel), and velocity magnitude and streamlines (right panel). Results for  $Re = 20$  and (a) water-water, (b)  $[AsA] = 0.85$  mol/L and  $[HCl] = 0.10$  mol/L, and (c)  $[AsA] = 1.7$  mol/L and  $[HCl] = 0.10$  mol/L.

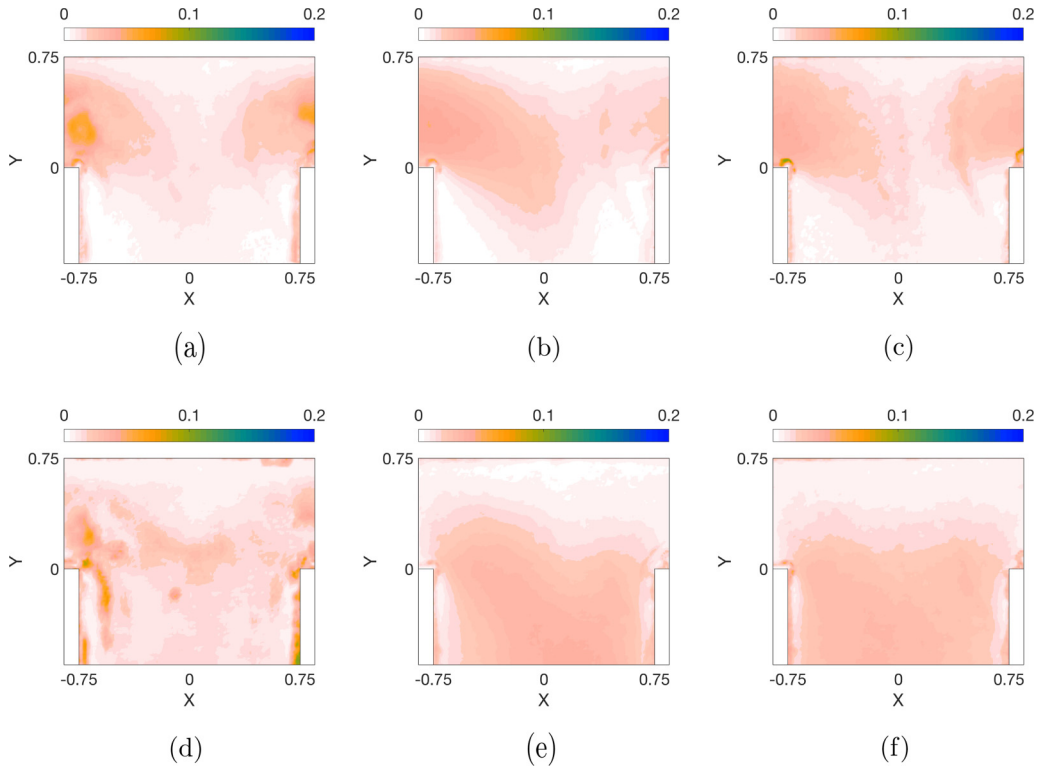


FIG. 6. Nondimensional random error on the velocity measurements. [(a)–(c)]  $x$ -velocity fields and [(d)–(f)]  $y$ -velocity fields. Results for  $Re = 20$  and [(a), (d)] water-water, [(b), (e)] [AsA] = 0.85 mol/L and [HCl] = 0.10 mol/L, and [(c), (f)] [AsA] = 1.7 mol/L and [HCl] = 0.10 mol/L.

vertical for the water-water case, tends to tilt as shown in Figs. 2(b) and 2(c), and thus the contact line between the two streams moves toward the lateral side of the mixer. In particular, the interface moves to the right side, going upward along the  $z$  direction [see Figs. 4(b), 4(c) 5(b), and 5(c)], because the aqueous solution of AsA, which enters from the right, due to its higher density, tends to flow into the lower part of the channel. The opposite occurs when moving to the bottom plane of the mixer. These effects of stratification become more significant as the density ratio increases, as we can see by observing the case with the highest concentration of ascorbic acid [see Figs. 4(c) and 5(c)]. Experimental measurements and numerical predictions are again in good agreement, as for all considered planes and working fluids the difference between predicted and measured velocities lie below a few percent when  $Re = 20$ .

The reproducibility of the PIV measurements was estimated by evaluating the random error for both the  $x$ - and the  $y$ -velocity distributions. For  $N = 50$  repeated measurements, the random error  $E$  is

$$E\left(\frac{U_x}{U}\right) = \frac{2\sigma(U_x)}{U\sqrt{N-1}}; \quad E\left(\frac{U_y}{U}\right) = \frac{2\sigma(U_y)}{U\sqrt{N-1}}, \quad (10)$$

where  $\sigma(U_x)$  and  $\sigma(U_y)$  are the standard deviations of the  $x$ - and  $y$ -velocity distributions.

As an example, Fig. 6 shows the results for the three couples of working fluids at  $Re = 20$  for the plane  $Z = 0.375$ . In all the velocity fields considered in this paper, locally the random error is less than 5% and, on average, it remains below 3%. The experimental measurements are therefore quite accurate, showing that the chosen number of realizations for each flow measurement is sufficient to obtain a satisfactorily resolution of the velocity field. The nondimensional random errors on the

velocity measurements for all the Reynolds considered in the present paper are included in the Appendix.

Figure 7 shows results for  $Re = 60$ , with the flow field still within the segregated regime. The incoming streams flow side by side along the mixing channel for the water-water case, as already described for  $Re = 20$  [compare Fig. 7(a) with Fig. 2(a)]. Instead, for the two cases with ascorbic acid, the two streams stratify along the mixing channel with the contact region gradually moving from vertical to horizontal. Looking at the first cross section of Figs. 7(c) and 7(e) at  $Y = -0.15$ , we notice that the contact region is vertical and practically identical to the one for the water-water case, except for a small S-shaped vortex. The experimental and numerical velocity-magnitude and streamlines fields in the confluence region, i.e., for  $-0.75 \leq Y \leq 0.75$ , for the plane  $Z = 0.375$  [left panels in Figs. 7(b), 7(d) and 7(f)] confirm that there are no significant differences between the three cases analyzed. This is because at the confluence of the inlet channels gravitational forces are negligible, so that the interface between the two inlet fluids is practically vertical even for the two cases with different concentrations of ascorbic acid. The effect of density difference is negligible even for  $Z = 0.525$ , shown in the central panels in Figs. 7(b), 7(d) and 7(f), while it becomes significant as we move down the mixing channel for the outermost horizontal plane [plane  $Z = 0.675$ , shown in the right panel in Figs. 7(b), 7(d) and 7(f)]. Moving toward the upper plane of the micro-device, it is noted that the small S-shaped vortex observed in the visualizations of the dye along the mixing channel determines a nonsymmetric velocity field. As for the quantitative differences between experiments and numerical simulations, again a good agreement is found.

At larger Reynolds numbers, the flow enters the so-called steady vortex regime, which is characterized by the presence of U-shaped vortical structures, stemming from two flow recirculation regions formed near the top wall. The legs of the U-shaped structures are counter-rotating and develop in the mixing channel. With a single fluid, these vortical structures are perfectly symmetric, i.e., they have the same intensity, thus leading to a flow field which is characterized by a double reflectional symmetry (see, e.g., Ref. [8]). Instead, Mariotti *et al.* [34] suggested that with different fluids, the different properties of the incoming fluids lead to different intensities of the legs with a consequent breaking of the double reflectional symmetry. This behavior was also noticed by Siconolfi *et al.* [30], who investigated the mixing behavior in a T-mixer fed with water but of different temperatures, thus with different viscosity. In such a case, since density differences were neglected, the legs of each U-shaped vortical structure had equal intensity, thus preserving a single reflectional symmetry. Conversely, the numerical simulations of Ref. [34] for  $[AsA] = 1.7$  mol/L suggested that with different fluids, the different properties of the incoming fluids cause an imbalance even between the intensity of the legs belonging to the same U-shaped structure.

Figure 8(a) and Figs. 8(c) and 8(e) show the nondimensional  $MB^+$  concentration in different cross sections of the mixing channel at  $Re = 100$  for water-water and for different concentrations of the ascorbic acid, respectively. In the former case, the contact region between the two streams remains perfectly vertical with poor mixing due to just diffusion. Conversely, in the latter cases, the contact region progressively bends from vertical to horizontal and presents an S curvature. The PIV and CFD flow fields in the T-junction head at  $Re = 100$  indicate that the effect of density difference is not so significant in that region; indeed, we notice only a slight asymmetry of the flow [compare Figs. 8(d) and 8(f) with Fig. 8(b)] with respect to the water-water case. The two recirculation regions near the top wall are present for all the considered working fluids, even though they are asymmetric in the case of density difference. The agreement between experimental and numerical predictions of the velocity field is satisfactory also in this case, with discrepancies of the order of 5% of the maximum speed, only in a few points reaching 10%. As for the reproducibility of the measurement, the random error is generally less than 4–5% with a maximum value of about 7% in some areas, for example, near the edges.

By further increasing the Reynolds number, the flow undergoes a steady engulfment regime in which the recirculation regions at the confluence of the inlet streams lead to a tilting of the top parts of the U-shaped vortical structures with one of the two legs of each vortical structure being more fed by the incoming fluid than the other. As a result, only the two strongest legs, which are corotating,

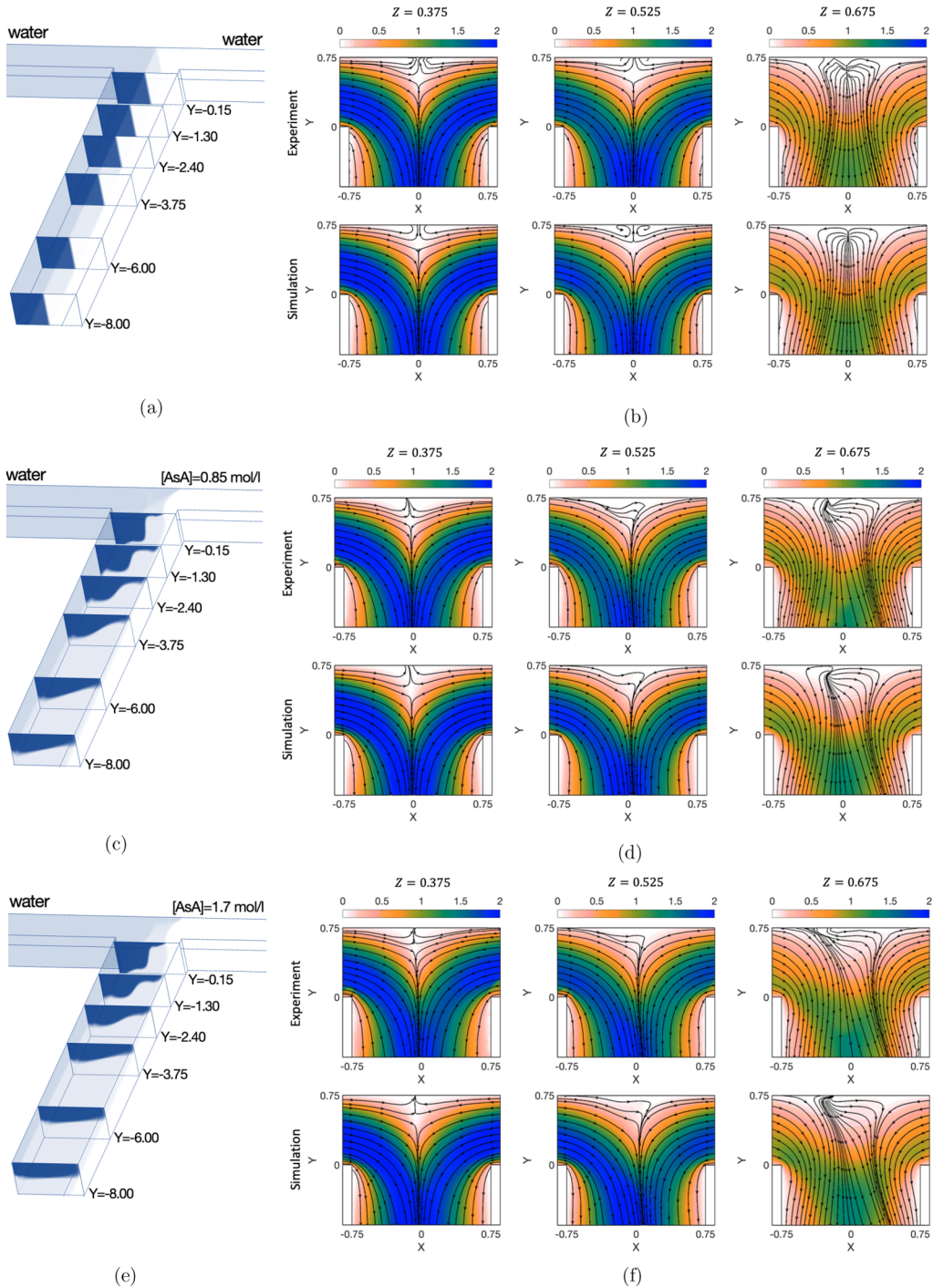


FIG. 7. [(a), (c), (e)] Nondimensional  $\text{MB}^+$  concentration in different cross sections of the mixing channel for  $-8 < Y < -0.15$  and [(b), (d), (f)] nondimensional velocity magnitude and streamlines experimentally measured (top) and numerically predicted (bottom) on the planes (from left to right)  $Z = 0.375$ ,  $Z = 0.525$ , and  $Z = 0.675$ . Results for  $\text{Re} = 60$  and [(a), (b)] water-water, [(c), (d)]  $[\text{AsA}] = 0.85 \text{ mol/L}$  and  $[\text{HCl}] = 0.10 \text{ mol/L}$ , and [(e), (f)]  $[\text{AsA}] = 1.7 \text{ mol/L}$  and  $[\text{HCl}] = 0.10 \text{ mol/L}$ .

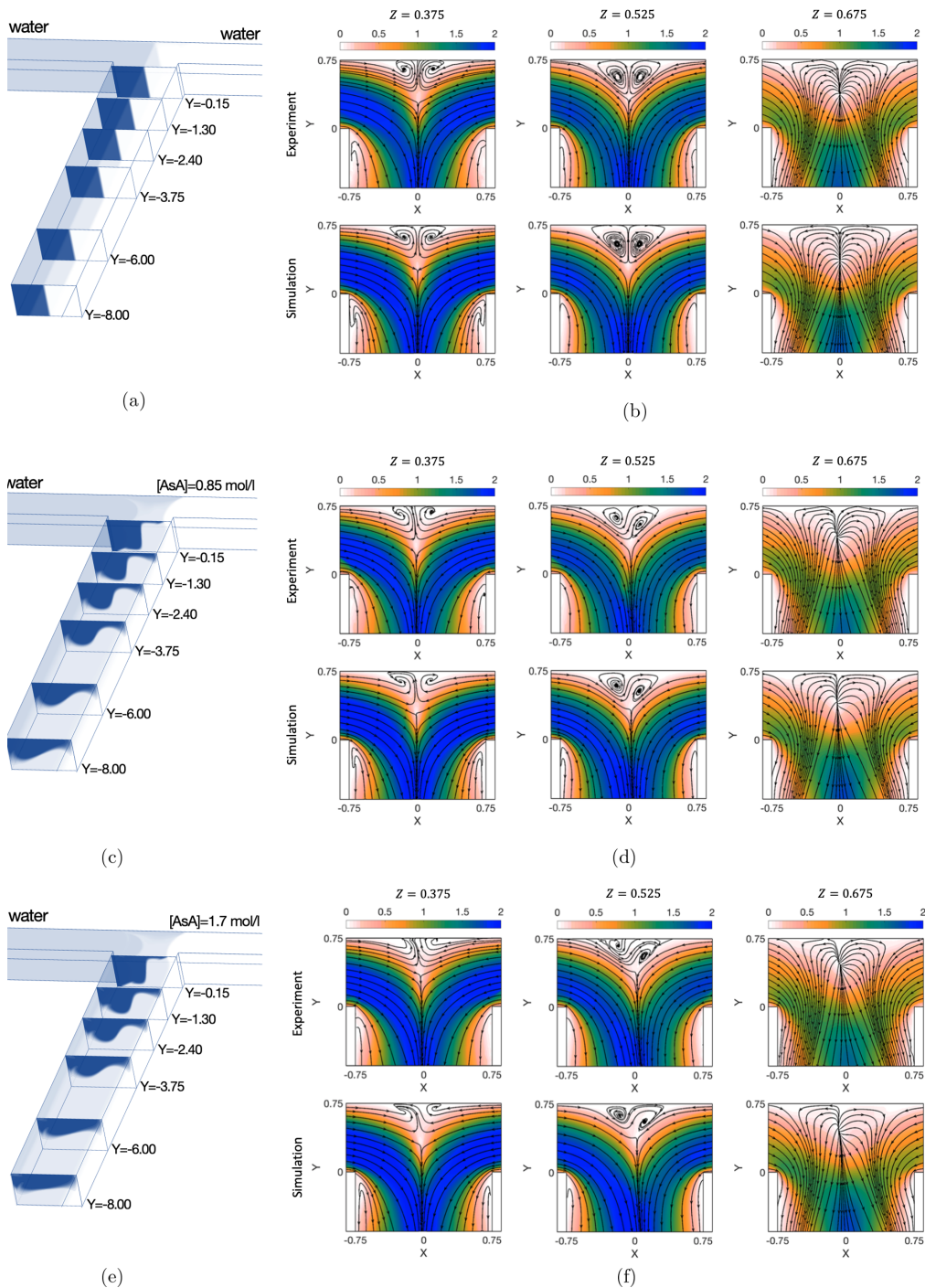


FIG. 8. [(a), (c), (e)] Nondimensional  $MB^+$  concentration in different cross sections of the mixing channel for  $-8 < Y < -0.15$  and [(b), (d), (f)] nondimensional velocity magnitude and streamlines experimentally measured (top) and numerically predicted (bottom) on the planes (from left to right)  $Z = 0.375$ ,  $Z = 0.525$ , and  $Z = 0.675$ . Results for  $Re = 100$  and [(a), (b)] water-water, [(c), (d)]  $[AsA] = 0.85$  mol/L and  $[HCl] = 0.10$  mol/L, and [(e), (f)]  $[AsA] = 1.7$  mol/L and  $[HCl] = 0.10$  mol/L.



survive further away in the mixing channel, while the two weakest legs rapidly vanish. This behavior enhances mixing through convection and produces S-shaped flow patterns in cross sections of the mixing channel, with each inlet fluid stream being able to reach the opposite wall. Figure 9 refers to  $Re = 150$  and indicates that the cases with the aqueous solution of ascorbic acid behave alike the water-water case. The only difference is that, as previously observed in the numerical simulations of Mariotti *et al.* [34], here the intensities of the two weak and two strong legs are different from each other, due to the different properties of the inlet fluids [compare the S shapes in the channels of Figs. 9(a), 9(c) and 9(e)].

Indeed, although some stratification effects are present, as the aqueous solution of ascorbic acid (white color) tends to move toward the bottom of the mixing channel, it is less important than in the segregated and vortical regime, since here convective effects dominate. This is confirmed by the experimental velocity fields and streamlines that are reported in Figs. 9(b), 9(d) and 9(f), where the recirculations near the top wall of the micro-reactor are clearly visible. These recirculations are almost the same for the three different density ratios and in all cases are significantly stronger than the ones found in the vortex regime [compare Figs. 9(b), 9(d) and 9(f) with Figs. 8(b), 8(d) and 8(f)].

## V. DIMENSIONAL ANALYSIS

As it appears from the last terms on the right-hand side of Eq. (4), the importance of stratification can be estimated through the Richardson number,

$$Ri = \frac{gd\Delta\rho}{\rho_0 U^2}, \quad (11)$$

expressing the ratio between buoyancy and inertial forces (often the Richardson number is referred to as the inverse square of the Froude number). Clearly, we see that

$$Ri = \frac{Gr}{Re^2}, \quad (12)$$

where  $Gr = \frac{gd^3}{\nu_0^2 \rho_0} \frac{\Delta\rho}{\rho_0}$  is the Grashof number, denoting the ratio between buoyancy and viscous forces. Hence, for a given  $Re$ , we notice that the significance of stratification depends on the characteristic size of the channel as  $Ri \propto d^3$ .

From the above discussion, it appears that the square root of the Grashof number plays the role of a transversal Reynolds number. Hence, we can define a transverse velocity (i.e., along the  $z$  direction) as

$$V_c = \frac{\nu_0}{d} \sqrt{Gr} = \sqrt{\frac{gd\Delta\rho}{\rho_0}}, \quad (13)$$

so that the Richardson number is related to the ratio between longitudinal and transversal velocities, i.e.,

$$Ri = \left(\frac{V_c}{U}\right)^2. \quad (14)$$

When a passive tracer spans a transversal distance  $\ell \approx d$ , it would move downward along the mixing channel by a distance  $L \approx dU/V_c$ , i.e.,

$$\frac{L}{d} \approx \frac{U}{V_c} = \frac{1}{\sqrt{Ri}}. \quad (15)$$

Clearly, at distances  $|y| < L$  from the confluence along the mixing channel, gravitational effects are negligible, while when  $|y| > L$  full stratification has been achieved. Finally, by substituting Eq. (13)

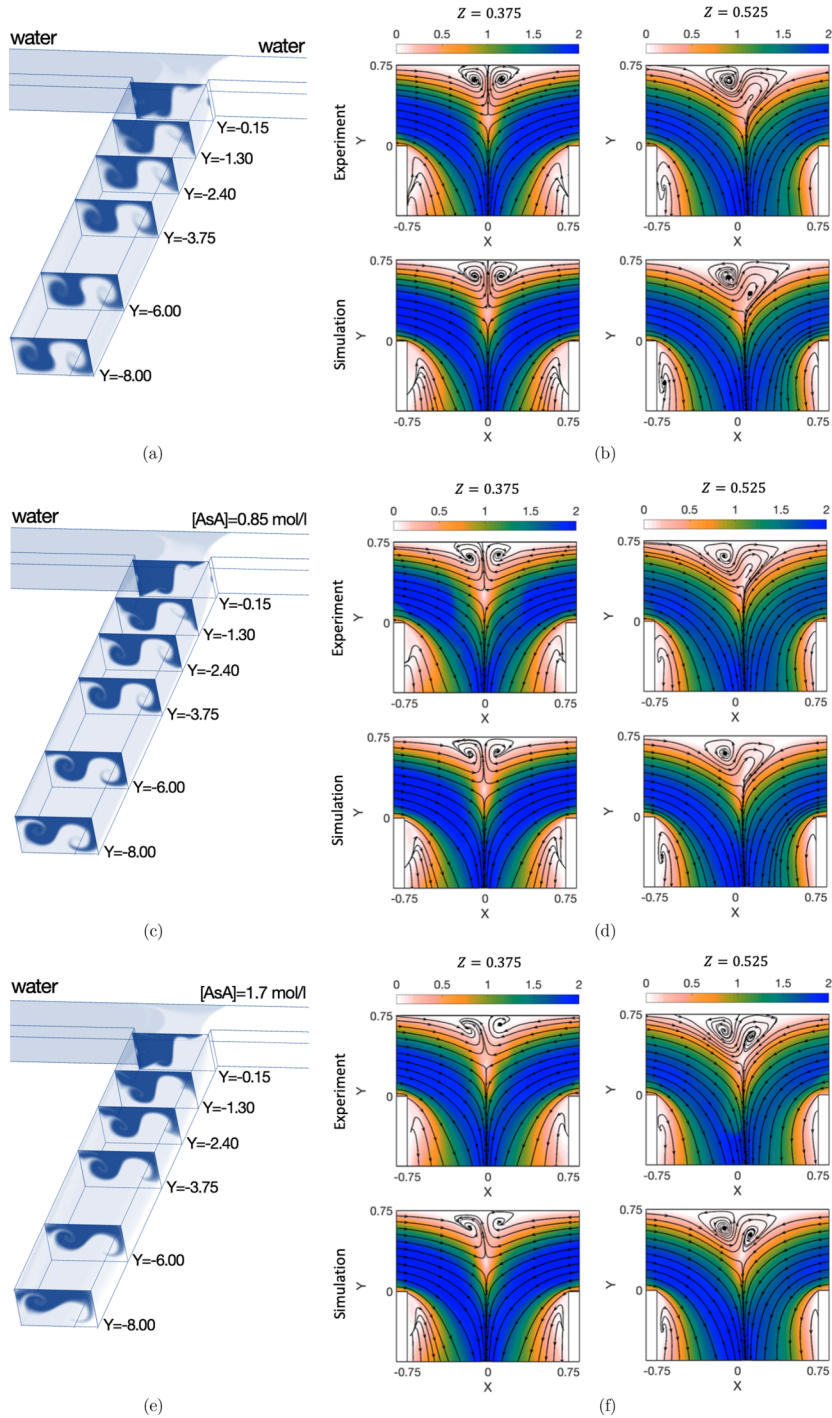


FIG. 9. [(a), (c), (e)] Nondimensional  $MB^+$  concentration in different cross sections of the mixing channel for  $-8 < Y < -0.15$  and [(b), (d), (f)] nondimensional velocity magnitude and streamlines experimentally measured (top) and numerically predicted (bottom) on the planes (from left to right)  $Z = 0.375$  and  $Z = 0.525$ . Results for  $Re = 150$  and [(a), (b)] water-water, [(c), (d)]  $[AsA] = 0.85$  mol/L and  $[HCl] = 0.10$  mol/L, and [(e), (f)]  $[AsA] = 1.7$  mol/L and  $[HCl] = 0.10$  mol/L.

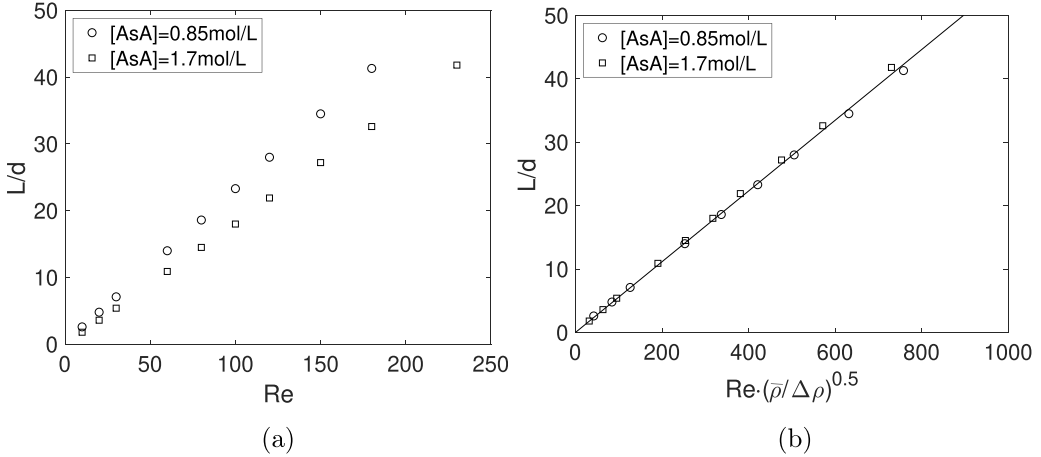


FIG. 10. (a) Stratification length vs Reynolds and (b) proposed fit:  $\frac{L}{d} = \left(\frac{av_0}{\sqrt{gd^3}}\right) Re \sqrt{\frac{\bar{\rho}}{\Delta \rho}}$ , with  $a = 8.5$ .

into Eq. (15), we find the following relation:

$$\frac{L}{d} = \left(\frac{av_0}{\sqrt{gd^3}}\right) Re \sqrt{\frac{\rho_0}{\Delta \rho}}, \quad (16)$$

where  $a$  is an  $O(1)$  nondimensional constant to be determined experimentally.

An analogous scaling analysis could be performed assuming that the mixture reference state corresponds to a homogeneous mixture with composition  $\bar{\phi}_{AsA}$ , therefore replacing  $\rho_0$  with  $\bar{\rho}$  and  $\mu_0$  with  $\bar{\mu}$ , where  $\bar{\rho} = \rho(\bar{\phi}_{AsA})$  and  $\bar{\mu} = \mu(\bar{\phi}_{AsA})$ .

Information on the distance at which stratification is completed can be gained from the numerical simulations. First, we need to define a criterion to assess stratification. The cross sections of the mixing channel were analyzed to estimate the depth-averaged concentration of the dye along the  $x$  direction. In the absence of stratification, i.e., with the interface region separating the two fluids being perfectly vertical, the depth-averaged concentration would be 1 for negative  $X$  and 0 for positive  $X$  coordinates. Conversely, a perfect stratification would ensure a depth-averaged concentration of 0.5 for all  $X$  values. In the present study, we consider the flow to be stratified if the depth-averaged concentration is within the range of  $\pm 2.5\%$  with respect to 0.5. The cross sections in the mixing channel were analyzed using the above-mentioned criterion to determine the position of a nearly complete stratification.

As for the segregated regime, we can consider, for instance, the simulations for  $Re = 20$  in Fig. 2(a), where stratification is complete at  $\frac{L}{d} = 4.8$  and  $\frac{L}{d} = 3.6$  for  $[AsA]=0.85$  mol/L and  $[AsA]=1.7$  mol/L, respectively. In fact, we indicate the ascorbic acid concentration, i.e.,  $[AsA]$ , with the subscripts 1.7 and 0.85, and Eq. (16) gives

$$\left(\frac{L_{1.7}}{L_{0.85}}\right) = \left(\sqrt{\frac{\bar{\rho}}{\Delta \rho}}\right)_{1.7} \left(\sqrt{\frac{\Delta \rho}{\bar{\rho}}}\right)_{0.85} \approx 0.79, \quad (17)$$

in good agreement with the numerical result, i.e.,  $L_{1.7}/L_{0.85} = 0.75$ .

Figure 10(a) summarizes the length estimated from the CFD simulations for the fluid streams to fully stratify, i.e.,  $L$  in Eq. (16), for different Reynolds numbers and density differences. We see that  $L$  is linearly dependent on  $Re$  for both concentrations of ascorbic acid, well in accordance with Eq. (16). Figure 10(b) reports such a length as a function of  $Re \sqrt{\frac{\bar{\rho}}{\Delta \rho}}$ : We observe that the curves related to the two ascorbic acid contents collapse on each other, thus confirming the validity of the scaling proposed in Eq. (16) with  $a = 8.5$  in the considered range of variation of  $[AsA]$ .

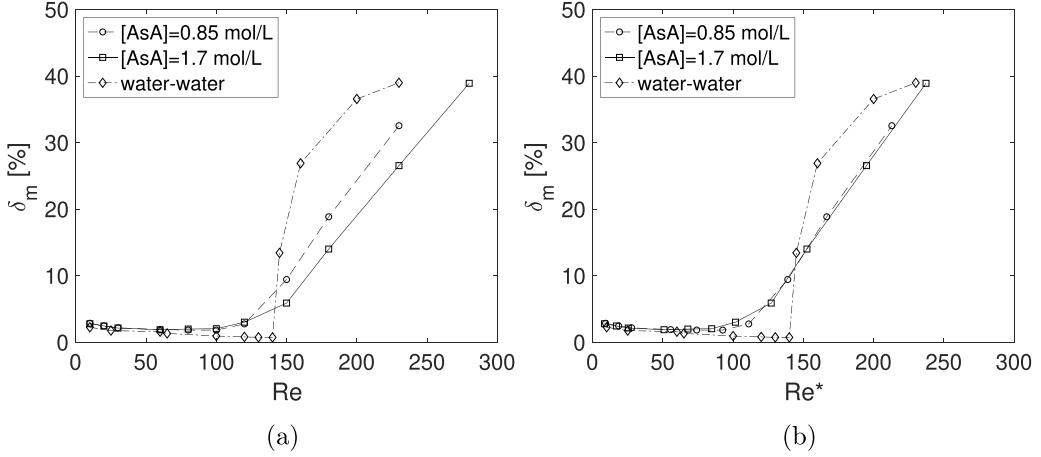


FIG. 11. Degree of mixing at the  $Y = -25$  cross section of the mixing channel as a function (a) of the Reynolds number  $Re$  and (b) of the modified Reynolds number  $Re^*$ . Data for the degree of mixing for the water-water case at the  $Y = -8$  cross section are from Ref. [12].

## VI. STRATIFICATION EFFECTS ON MIXING PERFORMANCE AND REACTION YIELD

To analyze how stratification influences the mixing process, Fig. 11(a) shows the degree of mixing  $\delta_m$  as a function of the Reynolds number for the three working fluids, whereas Fig. 12(a) summarizes the flow regimes as a function of the density ratio and of the Reynolds number. Here the degree of mixing,  $\delta_m$ , is defined as in Ref. [14], i.e.,

$$\delta_m = 1 - \frac{\sigma_b}{\sigma_{\max}}, \quad (18)$$

where  $\sigma_b$  is the standard deviation of the volumetric flow,

$$\sigma_b^2 = \frac{\int (\phi - \bar{\phi}_b)^2 u_y dx dz}{\int u_y dx dz}. \quad (19)$$

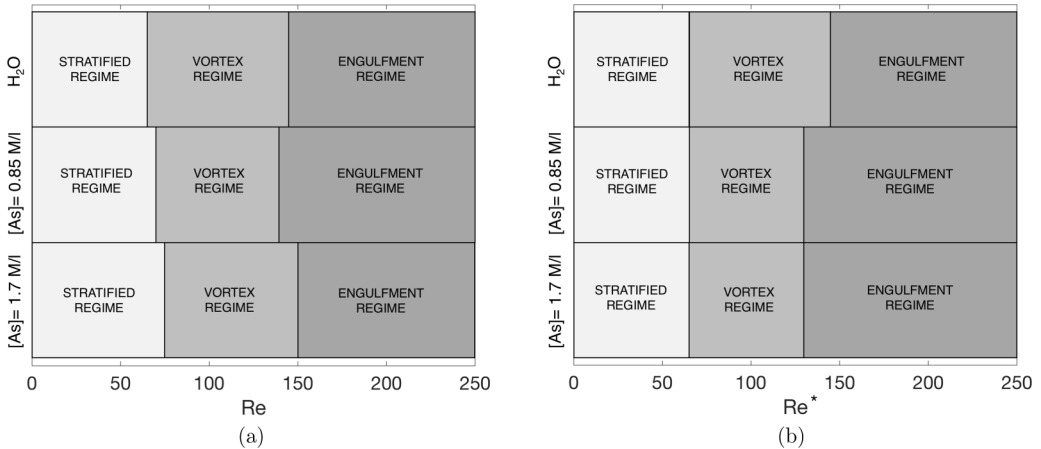


FIG. 12. Flow regimes as a function of the density ratio and of (a)  $Re$  and (b)  $Re^*$ .

Here,  $u_y$  is the  $y$  component of the velocity and  $\bar{\phi}_b$  is the bulk mass fraction,

$$\bar{\phi}_b = \frac{\int \phi u_y dx dz}{\int u_y dx dz}. \quad (20)$$

The maximum value of  $\sigma_b$  is denoted here with  $\sigma_{\max}$  and is obtained for completely segregated streams, resulting in

$$\sigma_{\max} = \sqrt{\bar{\phi}_b(1 - \bar{\phi}_b)}. \quad (21)$$

Accordingly  $\delta_m$  varies between  $\delta_m = 0$ , indicating a completely segregated flow, and  $\delta_m = 1$ , corresponding to a perfectly mixed flow.

To estimate  $\delta_m$ , we performed numerical simulations by using a negligible  $k_r$ , thus letting the methylene blue behave as a passive tracer. This setup allows us to overcome any ambiguity on the  $\delta_m$  calculation stemming from the presence of reaction products.

We notice that in the case of different inlet fluids, the degree of mixing at the  $Y = -25$  cross section of the mixing channel does no more increase suddenly at the onset of the engulfment regime; instead, it starts to rise gradually at Reynolds numbers significantly lower than the one of the transition to the engulfment regime. Indeed, in the vortex regime, the degree of mixing observed for different fluids is remarkably higher than that of the water-water case. This behavior originates from the stratification of the two inlet streams in the mixing channel. During such stratification, the contact region between the two streams crosses two of the four vortical structures occurring in the mixing channel in the vortical regime. As a consequence, convection affects the concentration field, thus enhancing mixing. This behavior is well visible in Figs. 7(c) and 7(e) at  $Re = 100$ , where we can notice a contact region between the two streams which presents some light blue puffs and is no more sharp than the segregated regime [see Figs. 2(b) and 2(c) at  $Re = 20$  or Figs. 7(c) and 7(e) at  $Re = 60$ ]. With increasing  $Re$ , the degree of mixing continues to increase monotonically in the engulfment regime, although with a slope which is higher than in the vortex regime but considerably lower than that of the water-water case. The rate of increase of the degree of mixing is similar for the two AsA concentrations, despite the fact that there is a shift of the curve toward higher  $Re$  values for the highest AsA concentration. We see that for different fluids  $\delta_m = 30\%$  is reached at remarkably higher  $Re$  numbers compared to the water-water case.

The degree of mixing along the axial direction  $|y|$  in the segregated regime is shown in Fig. 13(a), where the values of  $\delta_m$  at  $L/d$  are reported by using square symbols for  $[AsA] = 1.7$  mol/L and circular symbols for  $[AsA] = 0.85$  mol/L. In general, we see that in all cases  $\delta_m$  grows monotonically as we move down along the mixing channel, with a sudden increase near the confluence, when  $|y| < L$  and a slower linear growth in the sedimentation region, at  $|y| > L$ . For both values of  $[AsA]$  concentrations, the mixing degree curves collapse when the axial coordinate is divided by the stratification length  $y/L$ , as shown in Fig. 13(b). The slope of the curves in the sedimentation region, i.e., for  $|y| > L$ , is found to be a function only of the density and viscosity differences between the two inlet fluids, which, in turn, depend on the  $[AsA]$  concentration.

The effect of the stratification occurring at distances  $|y| > L$  from the confluence can be well described using the effective  $Re^*$ ,

$$Re^* = \frac{Ud}{\bar{\nu}}, \quad (22)$$

where  $\bar{\nu}$  is the kinematic viscosity of the homogeneous mixture of the two working fluids. In contrast, in our simulation we used the Reynolds number  $Re$ , which is defined in terms of the kinematic viscosity of pure water, as it better describes the convection that takes place near the confluence, when  $|y| < L$ . Therefore, it is not surprising that the curves related to the two AsA contents collapse into each other when plotting the degree of mixing as a function of  $Re^*$  as in Fig. 11(b) and the range of occurrence of the steady flow regimes becomes the same for the different AsA concentrations in case  $Re^*$  is considered as in Fig. 12(b). The curves related to the two AsA

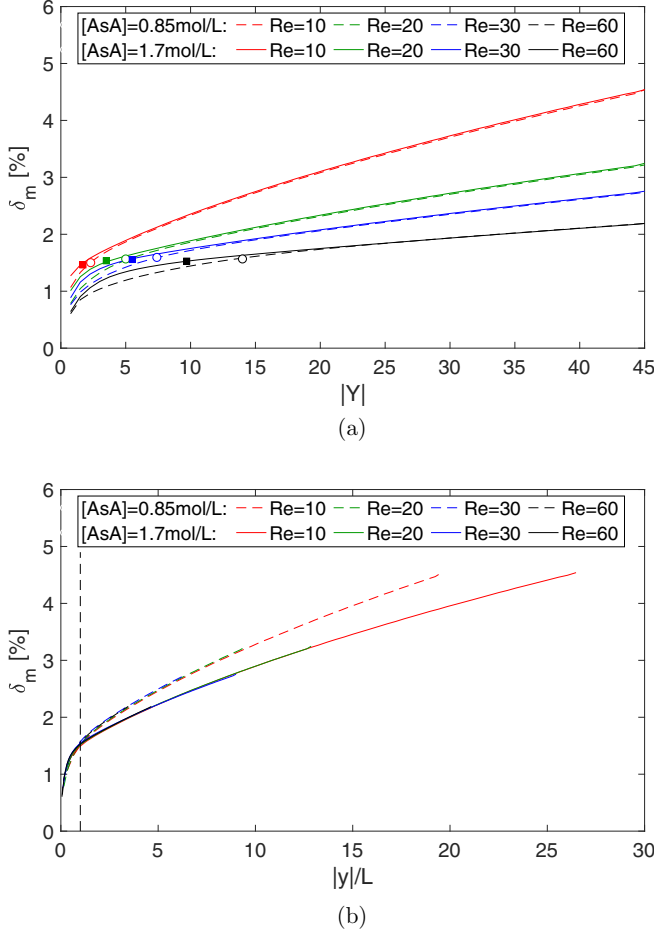


FIG. 13. Degree of mixing along the axial direction  $|y|$  in the segregated regime. Axial coordinate made nondimensional by using (a) the hydraulic diameter and (b) the stratification length  $L$ . The values of  $\delta_m$  at  $L/d$  are reported in panel (a) by using square symbols for  $[AsA] = 1.7$  mol/L and circular symbols for  $[AsA] = 0.85$  mol/L.

contents are located above that of the water-water case in the vortex regime, while they are below the water-water curve in the engulfment regime. However, for  $Re^* \approx 230$  the different working fluids show similar values of the degree of mixing. Above this  $Re^*$  value, the flow becomes unsteady and time periodic for all cases.

The reaction yield is quantitatively estimated following Ref. [34], by using the methylene blue concentration. Accordingly, the reaction yield,  $\eta$ , is

$$\eta = 1 - 2 \frac{C_{BM^+,out}}{C_{BM^+,in}}, \quad (23)$$

where the  $C_{BM^+,out}$  and  $C_{BM^+,in}$  are the methylene blue concentrations averaged at  $Y = -25$  and at the inlet, respectively. Figures 14(a) and 14(b) show the experimental and predicted values, respectively, of the reaction yield for all AsA and HCl concentrations. The  $[AsA] = 1.7$  mol/L case has been partly shown also in Ref. [34], where we highlighted the very satisfactory agreement between experimental and CFD yields. The additional cases provided here for the  $[AsA] = 0.85$  mol/L confirm the effect of the flow regime on the yield. Up to  $Re \approx 60$  (segregated regime),

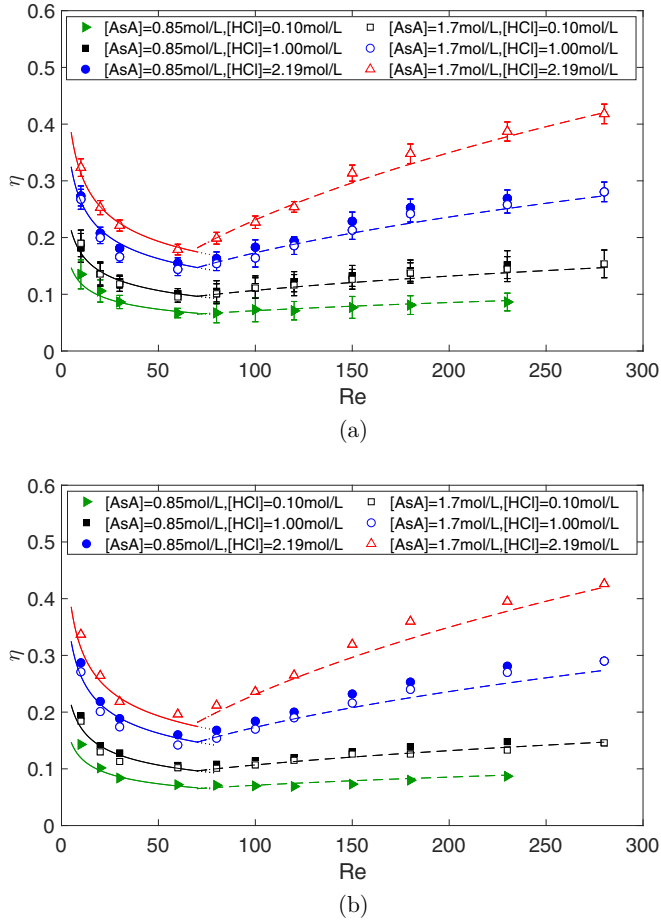


FIG. 14. (a) Experimental and (b) numerical reaction yield at the  $Y = -25$  cross section of the mixing channel as a function of the Reynolds numbers.

the reaction yield decreases with the Reynolds number, while in the vortex and engulfment regimes  $\eta$  augments with  $Re$ . As discussed in Ref. [34], we can explain this trend by figuring out how  $Re$  affects the contact area between the two streams and the residence time. These two factors determine, respectively, the mixing of reactants and the time available for the reaction to occur, thus ultimately affecting the reaction yield. In the segregated regime, the dominant effect is the reduction of residence time with the Reynolds number, as the contact area depends very weakly on  $Re$ . Conversely, the presence of vortical structures, whose strength increases with  $Re$ , affects remarkably the contact area in the vortex and engulfment regimes. Here, such an enhancement of the contact area with  $Re$  prevails over the reduction of residence time. The hollow and solid blue symbols refer to different combinations of AsA and HCl concentrations, leading, however, to the same value of the kinetic constant, i.e.,  $k_{r,0} = 2.60$  1/s (see Table I). We notice how the two data sets behave alike in all flow regimes, despite the  $\eta$  values obtained with the largest ascorbic acid concentration, i.e.,  $[AsA] = 1.7$  mol/L are slightly smaller than those for  $[AsA] = 0.85$  mol/L. This behavior is consistent with the hampering of the degree of mixing with increasing the density difference between the two incoming streams (see Fig. 11 and related discussion). The same observation holds for the hollow and solid black symbols, for which  $k_{r,0} = 10.71$  1/s.

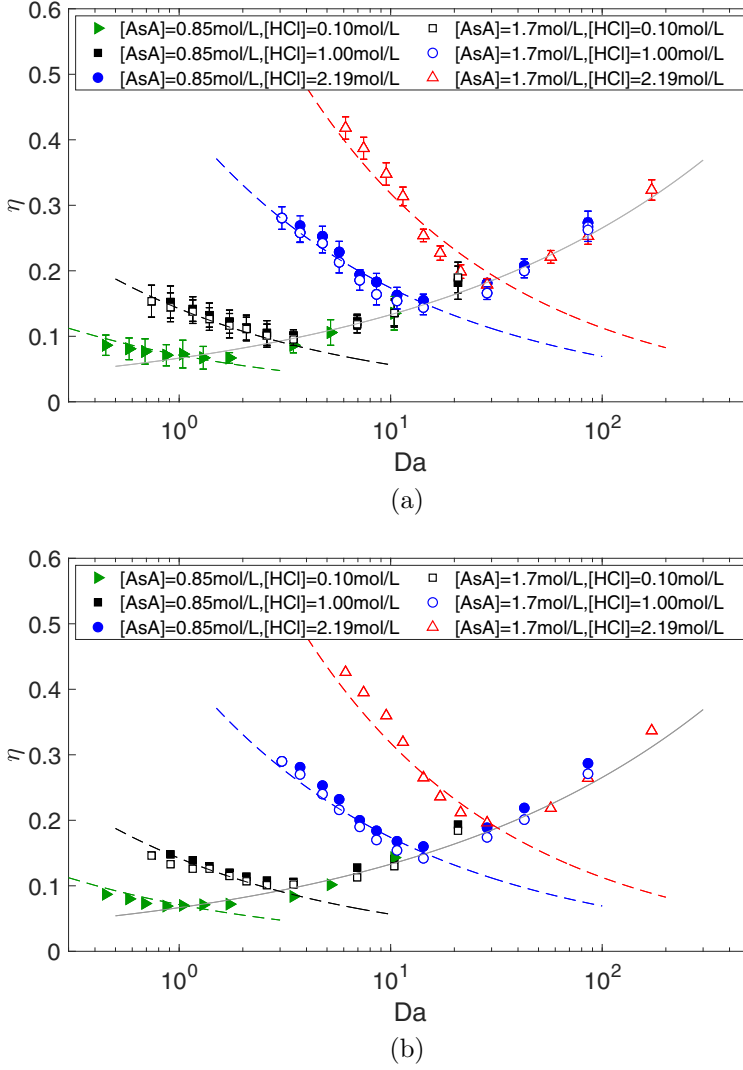


FIG. 15. (a) Experimental and (b) numerical reaction yield at the  $Y = -25$  cross section of the mixing channel as a function of the Damköhler numbers.

To better shed light on the role of flow regimes and kinetics on the reaction yield, Figs. 15(a) and 15(b) report the experimental and numerical yields, respectively, as a function of the Damköhler number, describing the residence to chemical timescale ratio, i.e.,  $Da = dk_{r,0}/U$ . In Ref [34], we showed that in the segregated regime (thus for large  $Da$ ), the yield depends solely on  $Da$  as

$$\eta \propto \frac{\widetilde{k}_{r,0}^{0.3}}{Re^{0.3}} \propto \widetilde{Da}^{0.3}. \quad (24)$$

Here,  $\widetilde{k}_{r,0}$  represents a nondimensional kinetic constant, i.e.,  $\widetilde{k}_{r,0} = k_{r,0} \frac{d^2}{\nu}$ , taking into account also fluid properties. Please note that this constant easily relates  $Da$  and  $Re$  as  $Da = \widetilde{k}_{r,0}/Re$ . This behavior is confirmed here also for different stratifications. Indeed, all curves [continuous lines in Figs. 14(a) and 14(b)], both experimental and numerical ones, collapse into each other and are well fitted by the above relationships [shown in Figs. 15(a) and 15(b) with a solid gray line], thus



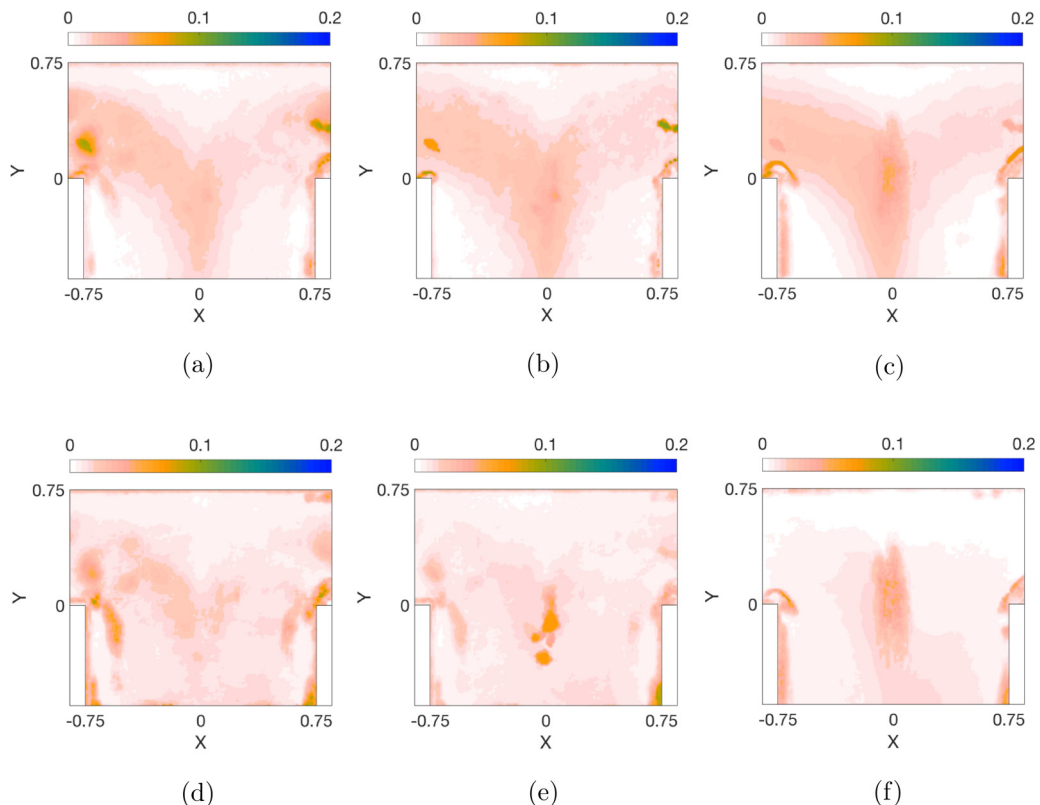


FIG. 16. Nondimensional random error on the velocity measurements. [(a)–(c)]  $x$ -velocity fields and [(d)–(f)]  $y$ -velocity fields. Results for  $\text{Re} = 60$  and [(a), (d)] water-water, [(b), (e)]  $[\text{AsA}] = 0.85 \text{ mol/L}$  and  $[\text{HCl}] = 0.10 \text{ mol/L}$ , and [(c), (f)]  $[\text{AsA}] = 1.7 \text{ mol/L}$  and  $[\text{HCl}] = 0.10 \text{ mol/L}$ .

corroborating the absence of any explicit dependency on  $k_{r,0}$  at least within the investigated range of operating conditions. As for the vortex and engulfment regime, we observe how the curves related to different  $k_{r,0}$  are well separated, thus indicating the direct effect of kinetic constant on the reaction yield. The scaling proposed by Mariotti *et al.* [34] as

$$\eta \propto \tilde{k}_{r,0}^{0.5} \text{Re}^{0.4} \propto \frac{\tilde{k}_{r,0}^{0.1}}{\text{Da}^{0.4}} \quad (25)$$

holds for all conditions investigated in the present work, as can be seen from the dashed lines in Figs. 15(a) and 15(b).

## VII. CONCLUSIONS

We have used experiments and numerical simulations jointly to study the effect of stratification as it may play a non-negligible role in case of density difference between the fluids to be used in practice or for quite large devices (approaching the millimeter scale). To this purpose, we have set up several operating conditions. We have considered kinetic constant values ranging from  $1.3$  to  $21.43 \text{ s}^{-1}$ . On the other hand, we also managed to get the same kinetic constant with different density ratios to single out the effect of stratification. Experiments consisted of PIV measurements, performed to determine the flow field in different horizontal planes of the micro-reactor, as well as flow visualizations. As for the latter, we used two different arrangements to gain information on the

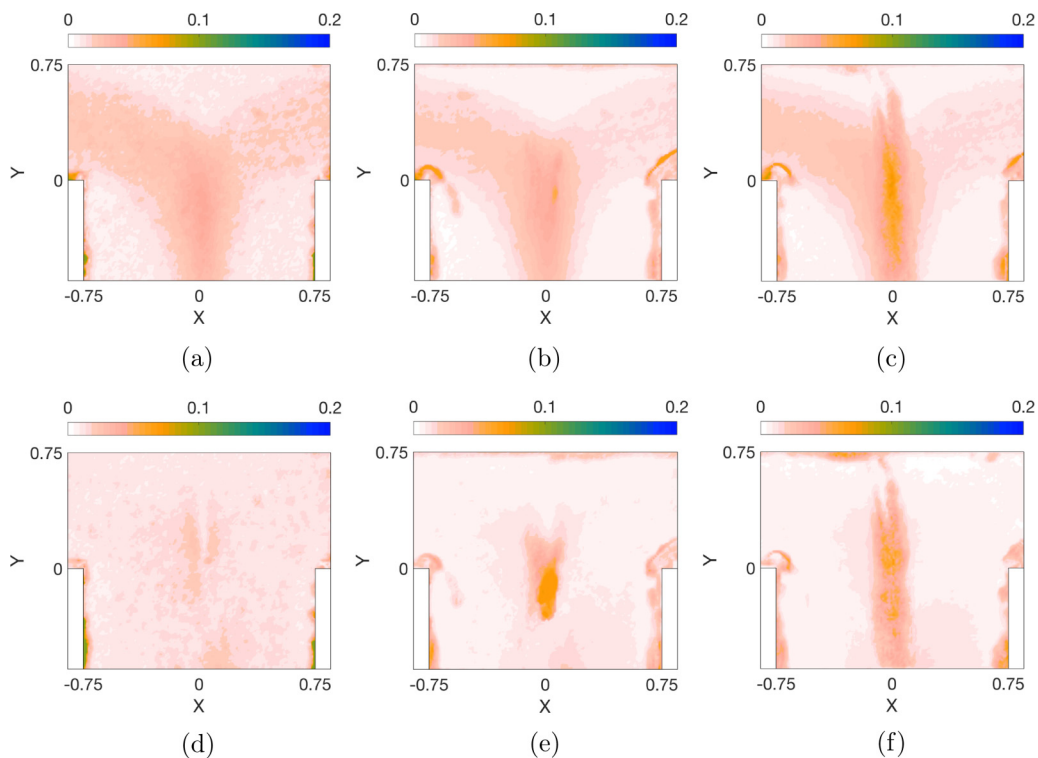


FIG. 17. Nondimensional random error on the velocity measurements. [(a)–(c)]  $x$ -velocity fields and [(d)–(f)]  $y$ -velocity fields. Results for  $Re = 100$  and [(a), (d)] water-water, [(b), (e)]  $[AsA] = 0.85$  mol/L and  $[HCl] = 0.10$  mol/L, and [(c), (f)]  $[AsA] = 1.7$  mol/L and  $[HCl] = 0.10$  mol/L.

vortical structures in the T junction, characterizing the flow regimes, as well as the methylene blue concentration in the mixing channel, determining the reaction yield. Numerical simulations allowed completing the experimental scenario by providing detailed information on the concentration and velocity fields, thus allowing us to obtain quantitatively estimates of the degree of mixing. The agreement between predictions and measurements is very satisfactory for both velocity and reaction yield.

Stratification affects remarkably the flow topology in the segregated regime, with a contact region that progressively moves from a vertical to a horizontal orientation. In fact, balancing gravitational and inertial forces, we determine a characteristic distance  $L = d/\sqrt{Ri}$  from the confluence along the mixing channel, where  $d$  is the hydraulic diameter and  $Ri$  is the Richardson number. In general, at distances  $|y| \ll L$ , the influence of gravity can be neglected, while at  $|y| \gg L$  the two fluids are fully segregated. This estimate gives a simple way to predict whether the effects of stratification may be important for given device dimensions, feeding fluids and operating conditions. In particular, at the confluence of the inlet fluids, the flow field is the same as the one that we obtain when the two inlet fluids are identical. Then, in the segregated regime, the contact region separating the two fluids of the inlet streams remains vertical at distances  $|y| \ll L$  along the mixing channel while it becomes progressively horizontal at  $|y| \approx L$ . Also, in the vortex regime, stratification breaks the double mirror symmetry with a contact region crossing the vortical structures and hence promoting some convection. Indeed, in this regime stratification gradually enhances mixing, in contrast to the case of two identical inlet fluids. When  $Re$  further increases, the degree of mixing continues to grow in the engulfment regime where the strong convection promotes a significant mixing enhancement, while gravity plays a minor role. Hence, despite having a beneficial effect in the vortex regime, in

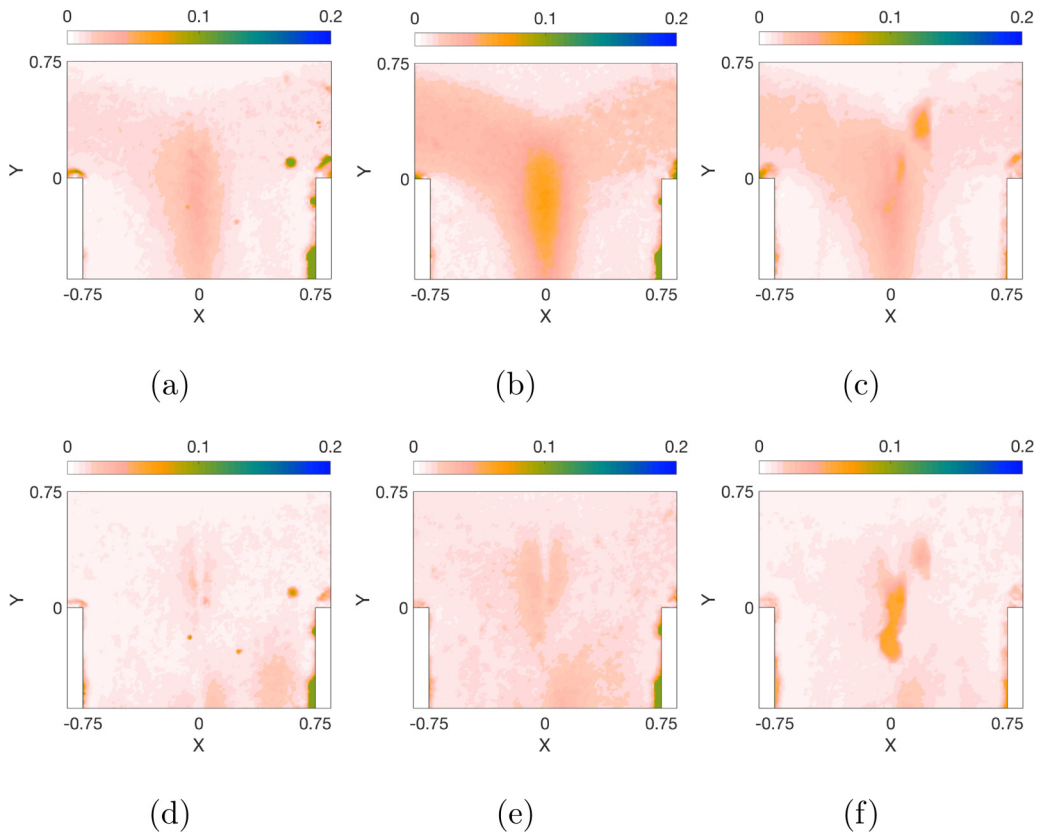


FIG. 18. Nondimensional random error on the velocity measurements. [(a)–(c)]  $x$ -velocity fields and [(d)–(f)]  $y$ -velocity fields. Results for  $Re = 150$  and [(a), (d)] water-water, [(b), (e)]  $[AsA] = 0.85$  mol/L and  $[HCl] = 0.10$  mol/L, and [(c), (f)]  $[AsA] = 1.7$  mol/L and  $[HCl] = 0.10$  mol/L.

the engulfment regime gravity-driven stratification hampers the sudden increase of the degree of mixing. As expected, the onsets of the vortex and engulfment regimes are delayed apparently upon increasing the density difference and hence the stratification effect; however, a proper definition of  $Re$  by using the homogeneous mixture properties of the two working fluids leads to similar behavior and similar  $Re$  values at the transitions from one regime to another.

As for the reaction yield, in the segregated regime, the residence time in the micro-reactor controls the reaction progress, so the residence to chemical timescale ratio is the dominant factor. Indeed, for all operating conditions, characterized by different stratification, we observed that the yield depends solely on the Damköhler number. In the vortex and engulfment regimes, the increase of mixing due to the enhanced convection dominates over the reduction of residence time with increasing  $Re$ . Besides, the yield depends more strongly on the kinetic constants, due to the vigorous mixing.

We believe that the present findings enlarge the comprehension of how stratification affects flow features, mixing as well as reaction yield. The proposed analyses, on the dependences of the degree of mixing on  $Re$  as well as of the reaction yield on  $Da$  and  $k_{r,0}$ , may be used to devise strategies for the practical operation of micro-reactors with fluids of practical interest. Clearly, further analyses would be useful to check the validity of the proposed scaling for density ratios or reaction rates outside the intervals considered herein. Furthermore, it would be interesting to investigate whether similar stratification effects are present also in reactors having different geometries.

**ACKNOWLEDGMENTS**

Support by the University of Pisa through the “Progetti di Ricerca di Ateneo PRA 2017-2018” funding program is gratefully acknowledged. Computational resources from CINECA computing center (Bologna, Italy) under ISCRA program (class B project “MIRE”) are also acknowledged. Finally, the authors are grateful to F. Porcu, A. Mastromarino, M. Antognoli, and C. Merello.

**APPENDIX: NONDIMENSIONAL RANDOM ERROR ON THE VELOCITY MEASUREMENTS**

The reproducibility of the PIV measurements was estimated by evaluating the random error for both the  $x$ - and the  $y$ -velocity distributions following Eq. (10). Figures 16, 17, and 18 show the nondimensional random error on the velocity measurements for  $Re = 60$ ,  $Re = 100$ , and  $Re = 150$ , respectively. The results are reported for the three couples of working fluids and for the plane  $Z = 0.375$ . As can be seen, in all the velocity fields considered in the paper, the random error is less than 5% (except for very few spurious localized values) and, on average, it remains below 3%. The experimental measurements are therefore quite accurate, showing that 50 realizations for each flow measurement are sufficient to obtain a satisfactorily resolution of the velocity field.

- 
- [1] I. Rossetti and M. Compagnoni, Chemical reaction engineering, process design and scale-up issues at the frontier of synthesis: Flow chemistry, *Chem. Eng. J.* **296**, 56 (2016).
  - [2] R. Gani, J. Baldyga, B. Biscans, E. Brunazzi, J.-C. Charpentier, E. Drioli, H. Feise, A. Furlong, K. M. Van Geem, J.-C. de Hemptinne, A. J. B. ten Kate, G. M. Kontogeorgis, F. Manenti, G. B. Marin, S. S. Mansouri, P. M. Piccione, A. Pova, M. A. Rodrigo, B. Sarup, E. Sorensen, I. A. Udugama, and J. M. Woodley, A multi-layered view of chemical and biochemical engineering, *Chem. Eng. Res. Des.* **155**, A133 (2020).
  - [3] T. Van Gerven and A. Stankiewicz, Structure, energy, synergy, time: The fundamentals of process intensification, *Ind. Eng. Chem. Res.* **48**, 2465 (2009).
  - [4] M. I. M. Al-Rawashdeh, F. Yu, E. Rebrov, V. Hessel, and J. C. Schouten, Numbered-up gas-liquid micro/milli channels reactor with modular flow distributor, *Chem. Eng. J.* **207–208**, 645 (2012).
  - [5] L. Fullin, E. Melloni, and A. dos S. Vianna Jr., Solution styrene polymerization in a millireactor, *Chem. Eng. Process.: Process Intensif.* **98**, 1 (2015).
  - [6] M. Ricconi, F. Alberini, E. Brunazzi, and D. Vigolo, Ghost particle velocimetry as an alternative to  $\mu$ PIV for micro/milli-fluidic devices, *Chem. Eng. Res. Des.* **133**, 183 (2018).
  - [7] A. Woitalka, S. Kuhn, and K. F. Jensen, Scalability of mass transfer in liquid-liquid flow, *Chem. Eng. Sci.* **116**, 1 (2014).
  - [8] S. Camarri, A. Mariotti, C. Galletti, E. Brunazzi, R. Mauri, and M. V. Salvetti, An overview of flow features and mixing in micro T and arrow mixers, *Ind. Eng. Chem. Res.* **59**, 3669 (2020).
  - [9] A. Fani, S. Camarri, and M. V. Salvetti, Investigation of the steady engulfment regime in a three-dimensional T-mixer, *Phys. Fluids* **25**, 064102 (2013).
  - [10] C. Galletti, A. Mariotti, L. Siconolfi, R. Mauri, and E. Brunazzi, Numerical investigation of flow regimes in T-shaped micromixers: Benchmark between finite volume and spectral element methods, *Can. J. Chem. Eng.* **97**, 528 (2019).
  - [11] A. Mariotti, C. Galletti, R. Mauri, M. V. Salvetti, and E. Brunazzi, Steady and unsteady regimes in a T-shaped micro-mixer: Synergic experimental and numerical investigation, *Chem. Eng. J.* **341**, 414 (2018).
  - [12] A. Mariotti, C. Galletti, M. V. Salvetti, and E. Brunazzi, Unsteady flow regimes in a T-shaped micromixer: Mixing and characteristic frequencies, *Ind. Eng. Chem. Res.* **58**, 13340 (2019).
  - [13] N. Kockmann, T. Kiefer, M. Engler, and P. Woias, Convective mixing and chemical reactions in microchannels with high flow rates, *Sens. Actuators B* **117**, 495 (2006).
  - [14] C. Galletti, G. Arcolini, E. Brunazzi, and R. Mauri, Mixing of binary fluids with composition-dependent viscosity in a T-shaped micro-device, *Chem. Eng. Sci.* **123**, 300 (2015).

- [15] C. Galletti, E. Brunazzi, and R. Mauri, Unsteady mixing of binary liquid mixtures with composition-dependent viscosity, *Chem. Eng. Sci.* **164**, 333 (2017).
- [16] A. S. Lobasov, A. V. Minakov, V. V. Kuznetsov, V. Y. Rudyak, and A. A. Shebeleva, Investigation of mixing efficiency and pressure drop in T-shaped micromixers, *Chem. Eng. Process.: Process Intensif.* **134**, 105 (2018).
- [17] A. Mariotti, M. Lanzetta, G. Dini, A. Rossi, E. Brunazzi, R. Mauri, and C. Galletti, Influence of cross-sectional geometry on mixing in a T-shaped micro-junction, *Chem. Eng. Trans.* **74**, 955 (2019).
- [18] R. J. Poole, M. Alfateh, and A. P. Gauntlett, Bifurcation in a T-channel junction: Effects of aspect ratio and shear thinning, *Chem. Eng. Sci.* **104**, 839 (2013).
- [19] S. K. Reddy Cherlo and S. Pushpavanam, Effect of depth on onset of engulfment in rectangular microchannels, *Chem. Eng. Sci.* **65**, 6486 (2010).
- [20] A. Soleymani, H. Yousefi, and I. Turunen, Dimensionless number for identification of flow patterns inside a T-micromixer, *Chem. Eng. Sci.* **63**, 5291 (2008).
- [21] H. V. Babu, S. Satu, M. Haderlein, W. Peukert, and N. Verma, Numerical investigation of flow patterns and concentration profiles in Y-mixers, *Chem. Eng. Technol.* **39**, 1963 (2016).
- [22] A. Mariotti, C. Galletti, E. Brunazzi, and M. V. Salvetti, Steady flow regimes and mixing performance in arrow-shaped micro-mixers, *Phys. Rev. Fluids* **4**, 034201 (2019).
- [23] A. Mariotti, C. Galletti, E. Brunazzi, and M. V. Salvetti, Unsteady flow regimes in arrow-shaped micromixers with different tilting angles, *Phys. Fluids* **33**, 012008 (2021).
- [24] B. J. You, Y. Choi, and S. G. Im, Influence of adjusting the inlet channel confluence angle on mixing behaviour in inertial microfluidic mixers, *Microfluid. Nanofluid.* **21**, 121 (2017).
- [25] S. T. Chan, J. T. Ault, S. J. Haward, E. Meiburg, and A. Q. Shen, Coupling of vortex breakdown and stability in a swirling flow, *Phys. Rev. Fluids* **4**, 084701 (2019).
- [26] N. Kockmann and D. M. Roberge, Transitional flow and related transport phenomena in curved microchannels, *Heat Transfer Eng.* **32**, 595 (2011).
- [27] G. Orsi, C. Galletti, E. Brunazzi, and R. Mauri, Mixing of two miscible liquids in T-shaped microdevices, *Chem. Eng. Trans.* **32**, 1471 (2013).
- [28] G. Orsi, M. Roudgar, E. Brunazzi, C. Galletti, and R. Mauri, Water-ethanol mixing in T-shaped microdevices, *Chem. Eng. Sci.* **95**, 174 (2013).
- [29] K. Ishii, S. Someya, and T. Munakata, Investigation of temperature-induced flow stratification and spiral flow in T-shaped microchannel, *Microfluid. Nanofluid.* **22**, 93 (2018).
- [30] L. Siconolfi, S. Camarri, and M. V. Salvetti, T-mixer operating with water at different temperatures: Simulation and stability analysis, *Phys. Rev. Fluids* **3**, 033902 (2018).
- [31] V. Hessel, H. Löwe, and F. Schönfeld, Micromixers—a review on passive and active mixing principles, *Chem. Eng. Sci.* **60**, 2479 (2005).
- [32] C. P. Holvey, D. M. Roberge, M. Gottsponer, N. Kockmann, and A. Macchi, Pressure drop and mixing in single phase microreactors: Simplified designs of micromixers, *Chem. Eng. Process.: Process Intensif.* **50**, 1069 (2011).
- [33] A. S. Lobasov and A. V. Minakov, Analyzing mixing quality in a T-shaped micromixer for different fluids properties through numerical simulation, *Chem. Eng. Process.: Process Intensif.* **124**, 11 (2018).
- [34] A. Mariotti, M. Antognoli, C. Galletti, R. Mauri, M. V. Salvetti, and E. Brunazzi, The role of flow features and chemical kinetics on the reaction yield in a T-shaped micro-reactor, *Chem. Eng. J.* **396**, 125223 (2020).
- [35] S. Mowry and P. J. Ogren, Kinetics of methylene blue reduction by ascorbic acid, *J. Chem. Educ.* **76**, 970 (1999).
- [36] M. G. Olsen and R. J. Adrian, Out-of-focus effects on particle image visibility and correlation in microscopic particle image velocimetry, *Exp. Fluids* **29**, S166 (2000).
- [37] M. Shamim and S. B. Khoo, Some physical properties of aqueous L-ascorbic acid solutions, *Aust. J. Chem.* **32**, 2293 (1979).
- [38] E. Nishikata, T. Ishii, and T. Ohta, Viscosities of aqueous hydrochloric acid solutions, and densities and viscosities of aqueous hydroiodic acid solutions, *J. Chem. Eng. Data* **26**, 254 (1981).